POLITECNICO DI TORINO

Master's Degree in Mechanical Engineering

Master's Degree Thesis

A Biomimetic Soft Pneumatic Actuator Inspired by the Chameleon's Ballistic Tongue Projection

Supervisors

Prof. Giuliana Mattiazzo

Prof. Parvez Alam

PhD. Fabio Carapellese

Candidate

Bruna Di Dato

April 2026

Acknowledgements

« Ancora che lo ingegno umano faccia invenzioni varie, rispondendo con vari strumenti a un medesimo fine, mai esso troverà invenzione più bella, né più facile, né più breve della natura, perché nelle sue invenzioni nulla manca e nulla è superfluo »

Leonardo da Vinci

This thesis was conducted at the University of Edinburgh, partially funded by a scholarship from Politecnico di Torino.

I would like to express my sincere gratitude to Prof. Mattiazzo for her unconditional trust, to Fabio for his constant and steady guidance, and to Prof. Alam, who, perhaps without realizing it, taught me a lot. I would also like to thank John Blackhurst for his warm welcome and his generous help.

I am deeply grateful to my parents because without their dedication and trust this thesis would never have taken shape. I'm also grateful to my brother, whom I've always looked up to; to Vincenzo for not always taking my side but offering his honest truth.

As this degree program comes to an end, my profound thanks go to all the good friends I've met along the way, with whom I had the privilege to share this adventure and many others to come.

Finally, I wish to dedicate this work to Emma Strada who, nearly one hundred and twenty years ago, at the very same university I now attend, opened the way as a pioneer.

Abstract

Biological organisms have long served as a source of inspiration for the design of artificial systems. The ability of animals, plants, fungi, and above all nanoscale organisms to adapt to different environments is the evidence for a highly specialized evolutionary structure. Among these, the chameleon's tongue exhibits remarkable characteristics in terms of speed and precision during prey capture, clearly differentiating it from other reptiles.

This thesis adopts a biomimetic approach to develop a novel soft pneumatic actuator inspired by the chameleon's ballistic tongue projection. The research establishes a foundational engineering framework to investigate a specific biological question: the mechanical role of the hyolingual apparatus in elastic discharge efficiency. The study transitions from a detailed biological analysis to the iterative design of a robotic analogue. Through analytical and numerical evaluation of various unit-cell geometries, a hexagonal trapezoidal model was selected and fabricated using Ecoflex 00-30 silicone. A rigorous material characterization campaign was conducted, resulting in a calibrated Yeoh hyperelastic model validated through uniaxial tensile testing and Finite Element Modeling. The manufacturing phase addressed critical soft-robotic challenges, successfully implementing a co-curing strategy for seamless bonding and pneumatic fitting encapsulation, while identifying vacuum degassing and precise radial reinforcement as key areas for future optimization. Ultimately, this work provides a validated, modular platform, comprising a characterized material model, a reproducible fabrication process, and a functional FEM framework, ready for integration with a structural hyoid scaffold. Rather than a final optimized device, this thesis delivers a grounded starting point for the development of high-fidelity biomimetic systems capable of replicating and explaining the mechanics of ballistic biological motion.

Table of Contents

Chapter 1

Literature Review and Problem Definition

The present chapter provides a structured review of the existing literature on soft robotics, with particular emphasis on the bio-inspired branch of the field, within which the present thesis is situated. Soft robotics has emerged in recent decades as a rapidly evolving discipline and, by drawing inspiration from biological organisms, researchers have developed a new generation of robotic architectures capable of achieving complex, continuous motions with a reduced number of discrete actuated degrees of freedom.

The first section of this chapter reviews the principal materials, actuation strategies, and fabrication techniques employed in soft robotic systems, and presents a selection of representative case studies that illustrate the current state of the art. The focus is devoted to those solutions that share conceptual or functional analogies with the system developed in this thesis.

The second section examines the biological foundations of this system: the skeletal architecture of the hyoid bone, the musculature of the tongue, and the kinematics of ballistic prey capture. The explicit aim is to identify the morphological and functional design principles that motivate the soft-actuator concept proposed in this work. The analysis of the biological reference system is conducted not merely as a descriptive exercise, but as a methodological tool for abstracting the key performance parameters and structural strategies that will inform the design choices choices presented in this work, and may equally serve as a conceptual framework for future developments and further advancements of the project.

Figure 1.1: Picture of a Parson's Chamaleo capturing a prey.
Copyright Lanting/Corbis

1.1 Nature-inspired Soft Robots State of the Art

Soft robotics is an emergent research domain concerned with the realization of robotic systems and actuators built primarily from compliant, highly deformable materials. These materials exhibit mechanical properties that more closely approximate those of biological tissues than the rigid substrates typically employed in conventional robotic architectures.

The soft robotic field relies heavily on biomimetics (or biomimicry), a practice dating back to Leonardo da Vinci's 15th-century flying machine, inspired by the study of birds. It essentially translates functional principles observed in nature into engineering solutions or, as Janine Benyus, the scientist who popularized the term, defines it: "it is a new science that studies nature's models and then imitates or takes inspiration from these designs and processes to solve human problems" [1].

Biomimetic approaches are particularly interesting because biological organisms have evolved highly specialized structures to perform precise tasks. In biological organisms, soft structures are not only energy dampers but contribute actively to locomotion, manipulation, and sensing through tightly integrated material compliance, geometry, and actuation. This concept is sometimes referred to as *embodied intelligence* or *mechanical intelligence* [2, 3]. While bio-inspiration draws general ideas from nature, the biomimetic design specifically seeks to replicate the underlying mechanisms of functional behaviors. For instance, the rapid movement seen in the closing of a Venus flytrap, who has the fastest morphing speed in the botanical world [4], or the projectile strike of a mantis shrimp [5] provides critical insights into how soft systems can store and instantaneously release elastic energy[6]. This is indeed relevant to the study of the chameleon's tongue, where a structured elastic element is used for energy storage and rapid projection.

The practical advantages of soft bio-inspired robotic systems become particularly apparent in situations where conventional rigid systems are inadequate, such as in unstructured or confined environments, or in tasks requiring delicate physical interaction.

Medical robotics is perhaps the most compelling application domain: soft continuum robots have demonstrated the capability to navigate complex pathways with minimal tissue trauma, and pneumatically actuated devices have been employed as rehabilitation tools for patients with motor impairments [7].

In industrial contexts, soft grippers—already commercially available from companies such as Shmalz Group (former Soft Robotics Inc.), can handle fragile or irregularly shaped objects without inducing damage, a task that remains challenging for traditional rigid end-effectors [3].

Search and rescue operations, underwater exploration, and human–robot collaboration represent further domains in which soft robotic systems provide decisive advantages over their rigid counterparts [2].

1.1.1 Materials for Soft Robots and Actuation Mechanisms

Soft robots can be built from many different materials and actuation mechanisms, each offering a distinct combination of design scopes in terms of compliance, force output, response speed, or energy efficiency. Moreover, the selection of materials and the choice of actuation principle are typically not independent decisions, as both are strongly interrelated through the structural design of the actuator. It has to be kept in mind that choosing the material is crucial in how well a soft robot works, as the material often acts as both the structure and the actuator.

As mentioned before, soft robots require materials that can deform significantly without breaking, and that are safe to use near humans or biological tissues. The most common choices are silicone elastomers, hydrogels, and braided fabrics. Silicone elastomers are particularly popular because they combine low stiffness, high elasticity, and biocompatibility, making them easy to mold and reliable over many loading cycles [3]. Their elastic modulus typically falls in the range of biological soft tissues (10^{2}˘10^{9} Pa), which is orders of magnitude lower than metals or hard plastics. This property allows the robot to distribute contact forces over a large area, reducing the risk of damage to fragile objects or human skin. A key concept for material selection is the work energy density, which relates how much mechanical work a material can deliver per unit volume. Stiffer materials tend to have higher energy densities but are less compliant: for instance, acrylic dielectric elastomers reach around 150 kJ/m^3, while silicone-based ones stay near 10 kJ/m^3 [11]. Many soft materials are also viscoelastic, meaning they dissipate energy when deformed and this property is well described by the loss modulus. This is useful for damping vibrations and stabilizing motion, but it also means the robot may respond differently at different speeds.

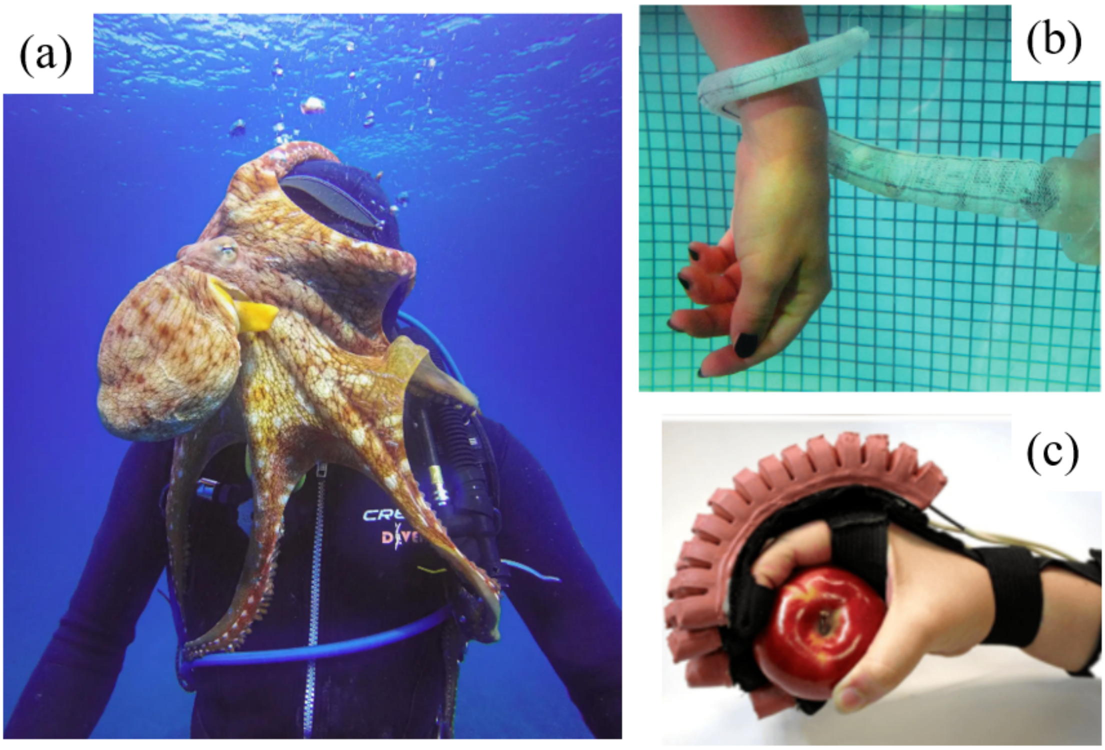

Figure 1.2: (a) An octopus grabs diver's face. Copiright by Caters News. (b) An octopus-like robot arm wrapping around a human wrist, in water. It is composed by an external braid that represent the mechanical structure of the arm, and a parallel of MA springs in the inside, that generate local diameter reductions. [8] (c) Soft penumatic glove for hand rehabilitation, an example of practical usages of soft robots. [9]

More recent innovations include Twisted and Coiled Polymer (TCP) actuators, which convert radial expansion into significant linear contraction, and origami-inspired structures. Origami-based designs utilize a compressible skeleton and a flexible skin to transform fluid pressure into complex multiaxial motions, such as bending, torsion, and contraction. These systems are highly scalable and can be

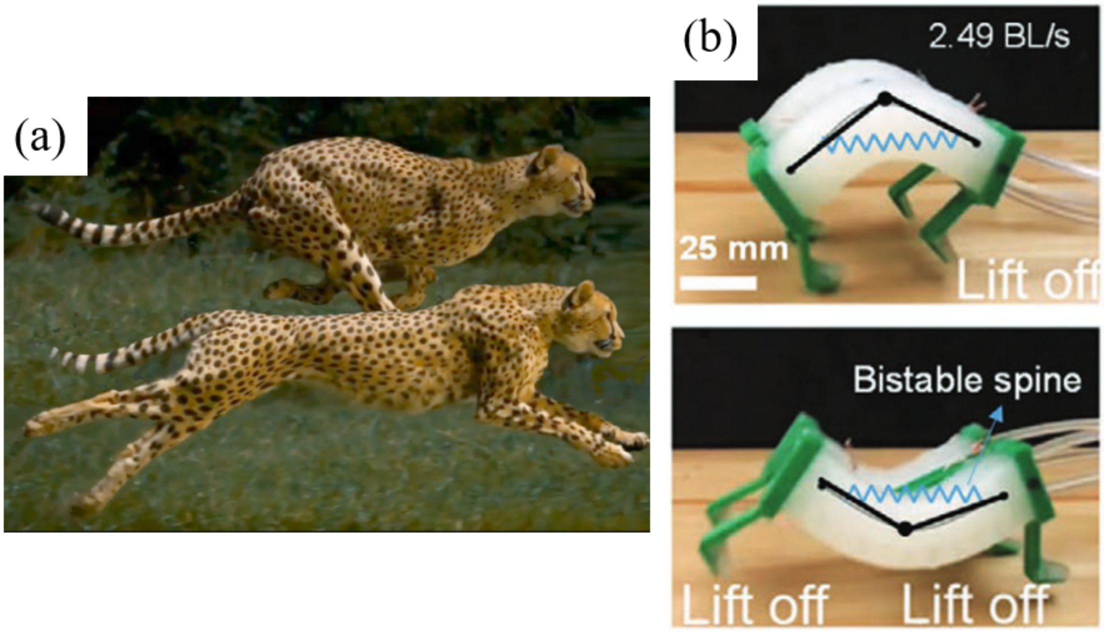

Figure 1.3: (a) key kinematic frames from the dynamic sequence of a galloping cheetah (b) A cheetah-inspired high-speed crawler featuring a bistable flexible spine mechanism with a pre-tensioned linear spring and two identical soft bending actuators, applied bistable structures concept, serving as skeletal muscles.[10]

programmed to achieve multiple degrees of freedom with minimal material cost but as a drawback they are easy to be vulnerable due to the repeated folding presenting a low reuse rate [7].

Moving a soft robot requires actuation strategies that work without rigid joints or motors. In terms of actuation mechanisms, three most widely used approaches are pneumatic/hydraulic actuation, shape memory alloys (SMAs), and dielectric elastomer actuators (DEAs).

Pneumatic systems, such as McKibben muscles, PneuNets, and fluidic elastomer actuators, use compressed air or fluid to inflate internal chambers in an elastomeric body, generating bending, elongation, or contraction [12, 13]. They are relatively simple to fabricate, can produce large forces, and allow continuous deformation with many degrees of freedom. However, they typically require external pumps and tubes, which limits portability. A notable step toward autonomous pneumatic robots is the "Octobot," a fully soft robot powered by an onboard chemical reaction of hydrogen peroxide that produces gas to drive its limbs without any rigid components [14].

SMAs, such as nickel-titanium (NiTi) alloys, contract when heated and are used as artificial muscles in many worm-like and caterpillar-like robots, including the Meshworm [15] and the GoQBot [16], shown in Fig. 1.4. In this sense, the properties of the material inherently also constitute an actuation system. They are compact and generate high forces relative to their weight, but their efficiency is thus very low (around 1%). DEAs actuate through electrostatic forces between compliant electrodes on either side of a soft membrane, producing large strains. Their performance is impressive in theory, but most designs require a rigid prestraining frame and operate at dangerously high voltages, complicating integration. Variable stiffness through particle jamming is another relevant actuation-adjacent mechanism: a flexible bag filled with granular material (such as coffee grounds) becomes rigid when a vacuum is applied, allowing the robot to switch between soft and stiff states for grasping or locomotion [17, 18].

Moreover, to achieve the explosive speeds sometimes necessary for biological mimicry, researchers are increasingly looking at elastic instabilities and buckling. An interesting application pf this concept is the use of a "stretch-attach-release" process or of bistable structures, with which designers can create actuators that snap between states, providing the rapid acceleration required for ballistic motions [19, 20].

In summary, considering the specific application addressed in this thesis, silicones offer the best balance of simplicity, cost, and performance for general soft robotics; Origami-based designs are more complex to manufacture but, they exhibit a very low structural mass, and their folding mechanisms enable an exceptionally high ratio between compressed and elongated configurations.

About actuation solutions, each method offers a trade-off: pneumatics are powerful but constrained, SMAs are compact but inefficient, and DEAs are versatile but electrically demanding.

1.1.2 Fabrication Methods

Producing soft robots involves techniques that are quite different from traditional machining. The most common approach is molding: liquid silicone or polyurethane is poured into a 3D-printed or CNC-machined mold, cured, and then assembled into the final structure. This process is accessible and inexpensive, but it requires multiple manual steps and makes it difficult to embed internal features like channels or sensors precisely.

Soft lithography [21], borrowed from microelectronics fabrication, allows the production of very fine internal channel networks in patterned elastomer (typically polydimethylsiloxane, PDMS), and has been used to create PneuNet actuators with

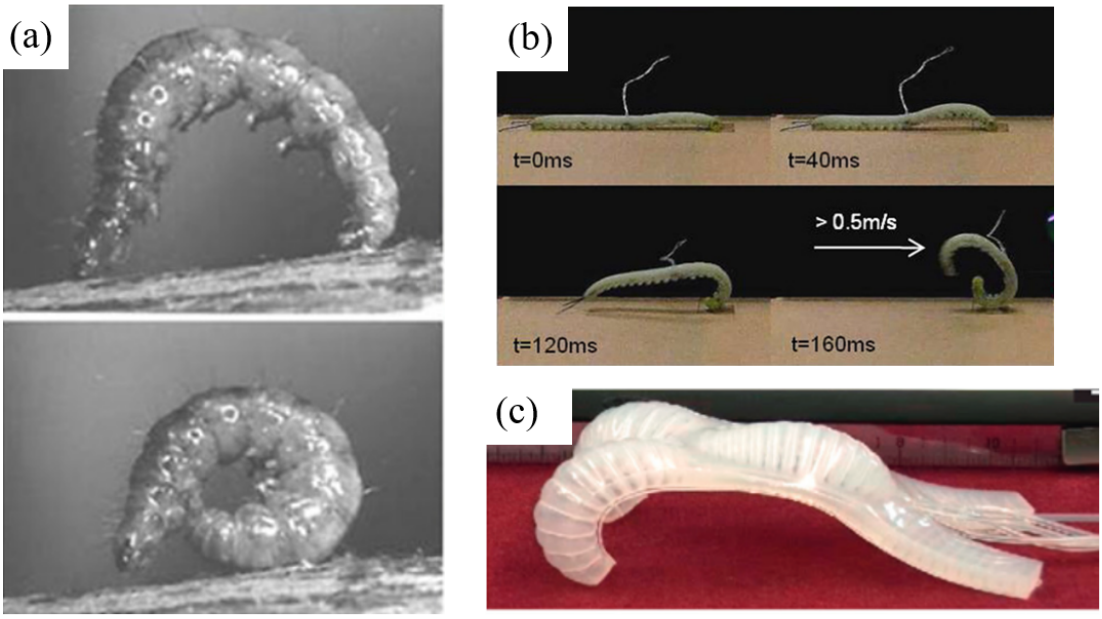

Figure 1.4: (a) Frame from a ballistic rolling escape maneuver in *Pleurupta ruralis*. Following a mechanical impact to the head while on the substrate, many leaf-roller caterpillars rapidly flex their bodies into a wheel to escape. Copiright by Macmillan Publishers Ltd: J Brackenbury Nature. (b) GoQBot, soft-bodied robot that simulates this ballistic rolling behavior, created using silicon and SMAs. [16]. (c) The Multigait soft robot, composed exclusively of soft materials fabricated by lithography and pneumatically actuated [12].

complex internal geometries [22]. This technique, however, presents drawbacks such as possible material deformation during the stamping process and the need for cleanroom environments to fabricate the initial master mold, limiting its flexibility for rapid prototyping of large-scale structures.

3D printing has become increasingly important because it allows direct fabrication of multi-material structures with embedded channels, sensors, and graded stiffness in a single step. For example, among the most interesting applications, Bartlett et al. [23] produced a combustion-powered soft robot with a functionally graded body (stiff at the core and soft at the outer shell) using 3D printing, something impossible to achieve with simple molding. Laser cutting and optical lithography have also been used to create regions of different stiffness in flat sheets that, when exposed to a solvent, fold into complex 3D shapes due to differential volumetric change — a technique called *strain-programmable matter* [24].

Bio-hybrid fabrication represents a more advanced frontier: living muscle cells (cardiac or skeletal) are grown directly on elastomeric substrates, acting as biological actuators. Nawroth et al. built an artificial jellyfish by patterning rat cardiomyocytes on a PDMS membrane, producing coordinated swimming motion. This approach is pioneering and powerful but requires cell culture infrastructure, sterile conditions, and careful biocompatibility testing, making it significantly more complex than purely synthetic fabrication routes.

Overall, molding remains the simplest and most accessible method; 3D printing adds geometric freedom at moderate complexity; and bio-hybrid techniques offer unique biological functionality at the cost of substantial manufacturing difficulty.

1.2 Biomimetical Approach: The Hyoglossal Apparatus of the Chameleon

The chameleon (order *Squamata*, family *Chamaeleonidae*) has attracted the interest of anatomists and functional morphologists for many years, and has been the subject of an unusually large number of experimental work. This interest is related not only from the animal's celebrated chromatic abilities or to its independently mobile eyes, but above all from the impressive ballistic performance of its tongue projection system.
In contrast to most other lizards, which have to move their whole body forward to catch prey, The chameleon typically remains stationary and projects its tongue over distances that can reach from approximately its full body length to as much as 2–2.5 times its body length in smaller and more specialized species, such as *Rhampholeon spinosus*, as reported by Anderson [25]. The high speed, accuracy, and energetic efficiency of this mechanism make it one of the most extraordinary feeding strategies found in vertebrates, and an almost uniquely interesting model for biomimetic engineering.

The question of which element of the hyolingual apparatus is the primary driver of the chameleon's extraordinary projection performance has been one of the most debated issues in the literature, and the debate has not been fully resolved.
Understanding this controversy is central to the motivation of the present thesis. Specifically, the ambiguity concerning the mechanical role of the hyoid bone—and its interaction with the hyoglossal complex—served as the main reason for designing a robotic system to isolate and quantitatively characterize this contribution in an experimental setting.
The present work therefore constitutes an initial step in that direction, beginning with the development of a tongue retractor prototype, which was undertaken in order to define and design all the principal components of the ballistic system.

1.2.1 Architecture and Roles in the hyolingual apparatus of the chameleon

The chameleon's tongue belongs to a larger system known as the hyolingual apparatus, which includes the tongue itself, the hyoid, the hyoglossus complex, and the extralingual muscles. Fig.1.5 presents a simplified schematic view of the chameleon's hyolingual apparatus, while Fig.1.6 shows a sectional view of the tongue, the entoglossal process, and the hyoglossus complex.

The tongue consists of the accelerator muscle, the collagenous intralingual sheaths (both responsible for the projection of the tongue) as well as the tongue pad, located at the tip and responsible for the catching of the prey, containing itself several muscles.

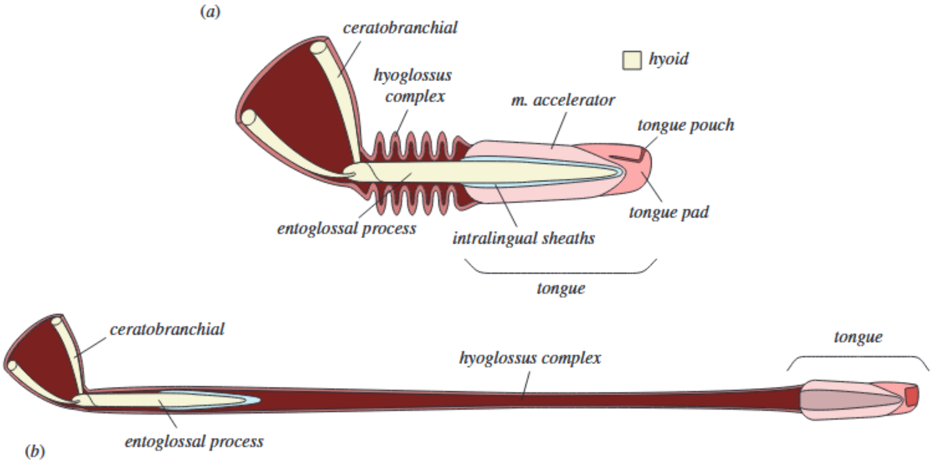

Figure 1.5: «Simplified schematic view of the functional anatomy of the hyolingual apparatus of the chameleon (a) and its configuration during projection (b).» [26]

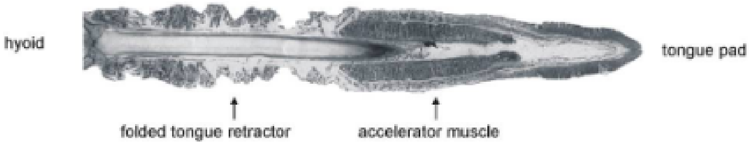

Figure 1.6: «Frontal section through the hyolingual apparatus of Chameleo jacksonii.» [27]

A thorough morphological and histochemical characterization of this system was provided by Herrel et al. [28], who identifies two dominant muscles, both in terms of mass and functional importance, that are the m. accelerator and the m. hyoglossus,

which together account for approximately 60–66% of total hyolingual muscle mass across species.
The entoglossal process also plays a particularly important role in the protrusion mechanism, as will be demonstrated below.

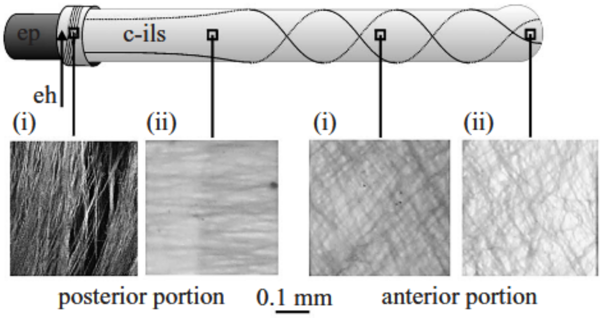

Figure 1.7: «Drawings of the main structure involved in the chameleon's tongue-projection mechanism and its fiber orientations along the sheaths.» [29]

The m. accelerator is a cylindrical muscle that envelops the entoglossal process. As shown in Fig.1.7 and Fig.1.8, the fibers are arranged in clockwise and anticlockwise spiral-shaped arcs [30], a configuration known to facilitate muscular elongation while constraining radial expansion [28], therefore allowing the muscle to stretch and contract by varying its diameter. As the m. accelerator contracts and its inner diameter decreases, it exerts a normal stress on the entoglossal surface that translates into a reaction force that propels forward the tongue pad. This results into a catapult effect in which the cylindrical tongue-muscle assembly slides along (and ultimately off) the entoglossal tip.

In the context of the entoglossal process, its functional significance is considerable because, in mechanical terms, it acts simultaneously as a guide rail, a force redirector, and an elastic loading substrate.

The hyoglossus complex, on the other end, constitutes the primary retractor system. As noted previously, the extrusion distances considered here can exceed the resting length of the muscles involved by several fold; the retractor muscles can indeed extend to over 17 times their contracted length [31]. The fibres of the m. hyoglossus are oriented approximately perpendicular to the muscle's longitudinal axis, and this architecture facilitates the substantial elongation that the muscle must undergo during maximal tongue projection.
Moreover, the hyoglossal complex is responsable to produce the slow radial contraction and axial loading that preloads the collagen springs.
To sustain force production, the retractor muscles of chameleons have evolved

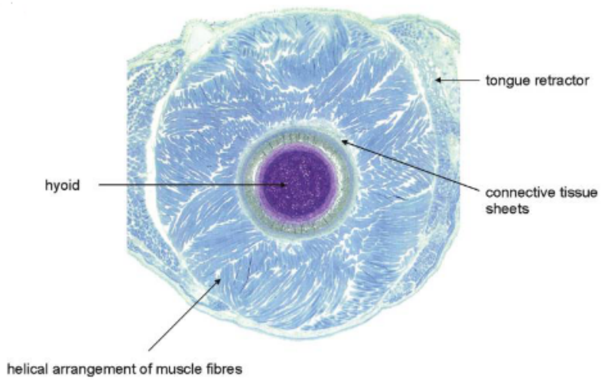

Figure 1.8: «Cross section through the hyolingual system in *Chameleo calyptratus* at mid tongue. Observe the dense centrally located cartilage of the entoglossal process, which is surrounded by layers of connective tissue and the helically wound accelerator muscle.» The tongue retractor fiber structure (m. hyoglossus) is also visible. [27]

supercontracting *sarcomeres*, a highly unusual structural specialization that distinguishes chameleon tongue retractors from those of most other vertebrates. For a more detailed discussion, the reader is referred to Ref. [27].

1.2.2 The Debate on Projection Efficiency and the Role of the Hyoid Bone

The historical debate over chameleon tongue projection highlights the complexity of attributing causal roles within an integrated musculoskeletal system, identifiying the precise triggering of ballistic release and how much the hyoid skeleton contributes to the tongue pad's total kinetic energy.

Early hypotheses, such as those by Brücke (1852) [33] and Gnanamuthu (1930) [34], unsure if the hyoglossus muscle acted as a passive retractor or as an active restraint during the loading phase. According to the latter hypothesis, the tongue would protrude only when the hyoglossus suddenly relaxed, releasing the constraint).
However, electromyographic and kinematic studies by Wainwright and Bennett (1992) [35] definitively identified the accelerator muscle as the primary agent of tongue loading. Their findings revealed that the hyoglossus activates too late to function as a restraint, while the accelerator exhibits a distinct biphasic pattern of storing and releasing energy, essential for generating the necessary tension prior to launch.

Quantitative modeling by Van Leeuwen (1997) [30] further refined this understanding by describing the accelerator as a muscular hydrostat. This model explains

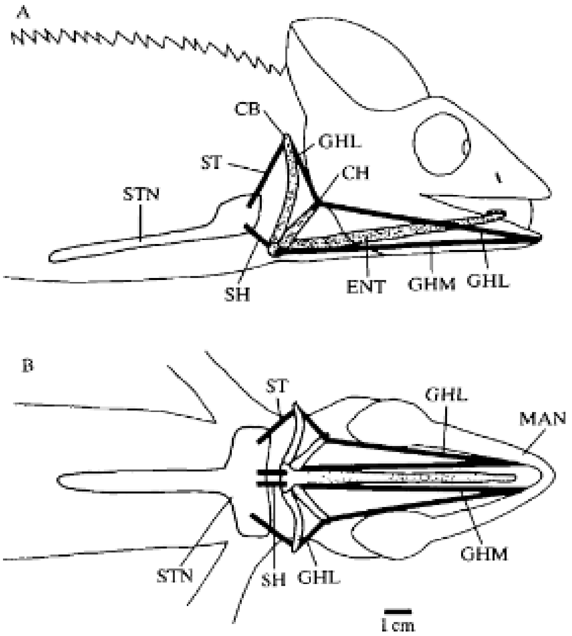

Figure 1.9: «Lateral (A) and ventral (B) schematic views of the head and hyobranchial structures of Chamaeleo oustaleti. Thick black lines indicate the attachments of the primary muscles. ACC, accelerator muscle; CB, ceratobranchial; CH, ceratohyal; ENT. entoglossal process; GHL, geniohyoideus lateralis muscle; GHM, geniohyoideus medialis muscle; MAN, mandible; RET, retractor muscle; SH, sternohyoideus muscle; ST, sternothyroideus muscle; STN, sternum.» [32]

how radial contraction is converted into axial force against the entoglossal process. Subsequent research by De Groot and van Leeuwen (2004) [29] introduced a critical discrepancy: according to the peak power recorded during projection exceeds, if the responsibility for the action had fallen on a muscle alone, it would have had to exceed the maximum theoretically possible size by 5–10 times. This suggests that the accelerator-entoglossal interaction is not merely a direct power source but part of a sophisticated elastic energy release mechanism involving intralingual connective tissues. Beyond the projection event itself, the hyoid apparatus serves a vital dual function. While its direct contribution to instantaneous power is less than 10%, its morphology is specialized for post-projection tasks. Due to the tongue's extreme specialization for ballistic strikes, it loses significant efficiency in prey transport. Consequently, the hyoid must compensate by driving intraoral repositioning, a functional shift that increases the duration and complexity of transport cycles compared to other lizards [27].

Finally, the fast protraction of the hyobranchial skeleton, characterized by the snap-through behavior of the ceratobranchial joints, has been proposed as a potential

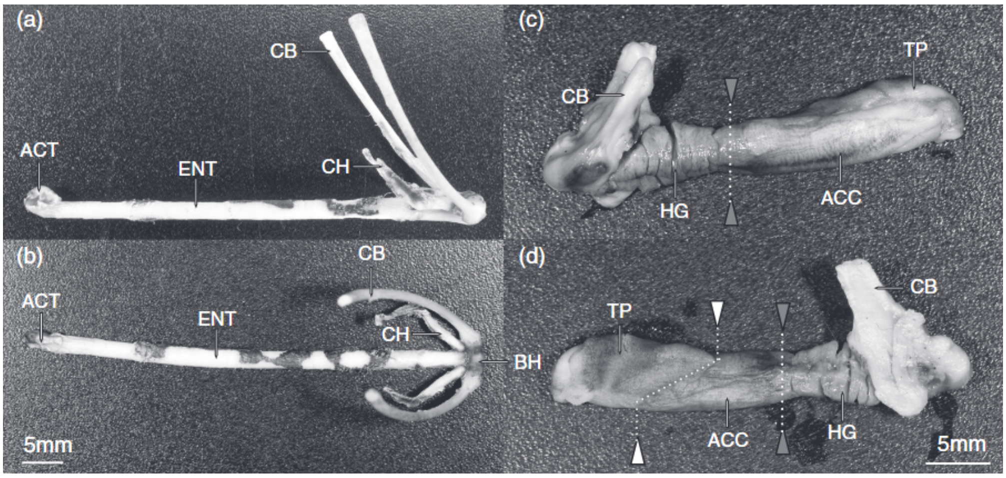

Figure 1.10: «Skeletal and muscular components of the chameleon tongue apparatus. Lateral (a) and dorsal (b) views of the skeletal elements of the tongue of C. p. parsonii. Ventrolateral (c) and dorsolateral (d) views of the muscular elements of the tongue of T.johnstoni at rest.» [36]

mechanical trigger for the release of the preloaded tongue [28]. However, since the precise influence of hyoid kinematics on the efficiency of elastic discharge remains experimentally unisolated, the debate on the specific role of the hyoid bone remains open.

1.2.3 Kinematics of Ballistic Prey Capture

High-speed cinematographic and video studies have provided quantitative descriptions of the full kinematic sequence of chameleon prey capture, which is very well captured in the video by the BBC presented at Ref.[37]. The sequence can be divided into four phases ([29],[32]): (I) slow tongue protrusion between the jaws; (II) rapid ballistic acceleration of the tongue toward the prey; (III) near-constant velocity flight; and (IV) deceleration, prey contact, adhesive capture, followed by retraction of tongue and prey into the mouth.

The kinematic data gathered by Wainwright et al. on Chamaeleo oustaleti remain among the most comprehensive in the literature. Tongue acceleration during phase II occurs in approximately 20 ms, reaching peak accelerations of up to 486 ms^{-2} and maximum velocities of 5.8 ms^{-1} for strikes at 35 cm. These values correspond to peak mass-specific power outputs on the order of 3000 Wkg^{-1}, consistent with the independently derived estimates of de Groot and van Leeuwen.

A notable kinematic feature is the simultaneous rapid forward protraction of the

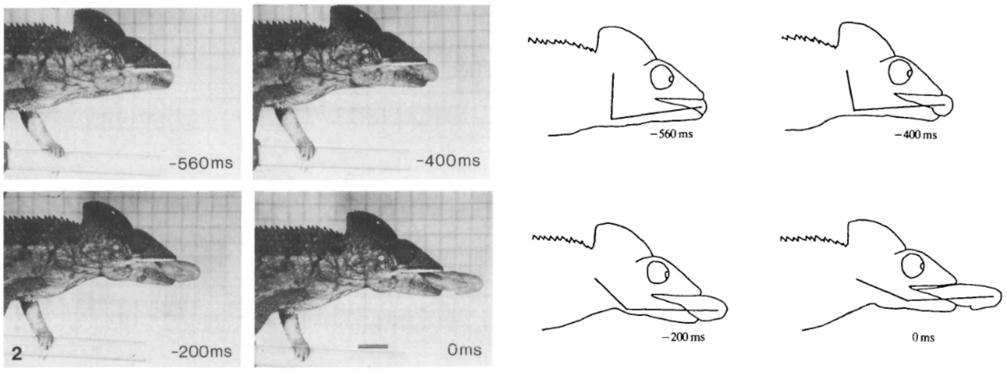

Figure 1.11: (On the left) «Four film frames of Chamaeleo oustaleti during the tongue protraction stage of prey capture that occurs prior to tongue projection. Scale bar, 2.0 cm. Note the gradual increase in gape and lack of whole-body movements as the tongue is protruded beyond the gape.» (On the right) «Tracings of the four film frames shown on the left, with the position of the hyobranchial bones in the throat as this structure is unfolded during tongue protraction.» [32]

entire hyobranchial skeleton at the onset of tongue projection, with average protraction velocities of approximately 0.7 ms^{-1}, which serves as a further evidence of the mechanical role of the hyoid in assisting projection.
The tongue decelerates and contacts prey within 5–10 ms, with retraction from full extension back into the mouth completed in an average of 251 ms at retraction velocities up to 2.99 ms^{-1}.

The chameleon does not require a body lunge toward prey, shows gape reduction rather than gape increase during tongue projection, and strongly depresses the head during retraction — features that distinguish it sharply from agamid lizards and represent specializations for a purely ballistic, high-reach capture strategy [32].

1.2.4 The Elastic Energy Storage Mechanism

Living organisms have developed advanced ways to store elastic energy that help them get around the basic limits of muscles, which contract too slowly and over too short a distance to create extremely fast movements on their own [5, 38]. Instead, many animals use a two-step strategy: muscles tighten slowly to load spring-like parts—such as tendons, outer body plates, or collagen layers—storing energy that is then released in a split second through latches or sudden shape changes, greatly boosting power. In the mantis shrimp's striking limb, for example, opposing extensor and flexor muscles work together to bend flexible outer structures—a tape-spring-like element and a saddle-shaped shell segment—held in place by small locking parts called sclerites. When the flexor muscles relax, the stored energy

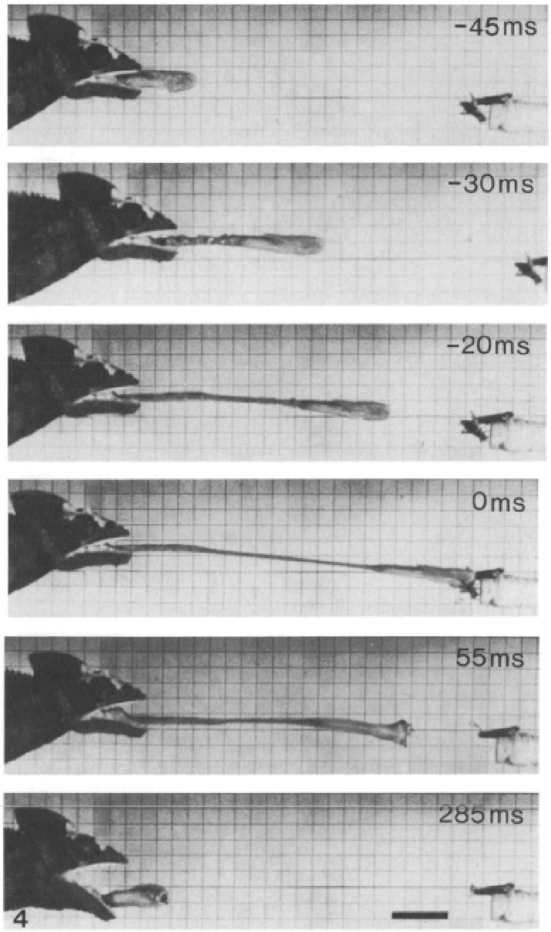

Figure 1.12: «Six frames of Chamaeleo oustaleti during tongue projection, prey contact and tongue retraction. Time zero is the time of prey contact. Frame —45 ms is the frame immediately prior to the onset of tongue projection. 15 ms later the tongue is traveling at over 3 ms^{-1}. Tongue retraction takes longer than projection, requiring almost 300 ms» [32]

is released and drives the striking segment (the dactyl) outward with extreme speed and force, far beyond what muscles alone could produce, even creating extra damage through cavitation bubbles in the water[39]. Nematodes show a similar idea using a reversible "kink" in their stiff skin: they slowly curl into a tight loop and then snap open almost instantly, launching themselves into the air and showing how passive body mechanics can move faster than active muscle contraction [38]. These biological "catapults" are powerful because they separate the slow phase of energy loading from the quick phase of release, allowing accurate, high-force movements for catching prey or escaping predators—especially in thick or resistant fluids—while also reducing muscle fatigue through efficient elastic recoil [5, 40]. A key case for bioinspired engineering, and the focus of your thesis, is the chameleon's projecting tongue: here, the spiral-shaped entoglossal muscle slowly tightens to stretch elastic collagen layers and build up internal fluid pressure, then triggers a rapid release that flings the tongue outward at very high speeds, with accelerations far above what gravity alone would allow—similar in principle to many other species that face comparable demands [5, 29]. The repeated use of this elastic catapult strategy across many groups of animals shows how reliable it is in evolution, making it a strong model for soft robotics, where small, fast-moving actuators can copy these fatigue-resistant systems for tasks like quick manipulation in confined spaces [41].

1.3 Overview of Analogous Designs Inspired by the Chamaleon Tongue

The extraordinary ballistic performance of the chameleon's tongue has inspired several research groups to develop robotic systems capable of replicating its speed, extensibility, and precision.
While the biological goal is common, the engineering approaches vary significantly, ranging from rigid catapulted systems to nested elastic structures. In this section, three key works are analyzed and compared. A summary can be found in Tab.1.1.
First work presented is by Debray (2011) [26]. This work presents four manipulators that strictly separate the projection system (using a coilgun or magnetic actuators) from the retraction system (based on a DC motor and an elastic "accordion" element). This study is very close to the biological model regarding kinematics, reaching accelerations of 573 m/s^2. The focus is on the dynamics of retraction and the use of elastomers to control speed.

Hatakeyama and Mochiyama (2013) [42] present a study on a shooting manipulation system, where an end-effector is launched by an impulsive air flow and connected by a flexible string. Unlike Debray's work, precision is guaranteed by a mechanical constraint (an elastic cantilever or an inertial wheel) that stops the movement at a specific point. This system showed a 92% success rate in capturing falling objects 0.7 m away.

The last work here presented is the one by Zheng et al. (2018) [43]. This paper focuses on a multi-layer nested structure to simulate the collagen muscles sheaths of the chameleon tongue. The approach is mainly based on dynamic modeling and 3D simulations in SolidWorks. They propose a mechanism for storing and releasing elastic energy to overcome the speed limits of standard soft grippers.

The three studies share three recurring design principles that reflect the core

Feature	**Debray (2011)**	**Hatakeyama & Mochiyama (2013)**	**Zheng et al. (2018)**
Projection Principle	Electromagnetic: Uses a coilgun to launch the tip.	Impulsive Pneumatic: High-pressure air blast.	Mechanical-Elastic: Rapid release of stored energy.
Retraction Mechanism	Hybrid: DC motor with elastic element.	Constrained: Nylon string with elastic cantilever.	Integrated: Nested elastic multi-layer structure.
Manuf. Complexity	**High:** Requires complex circuits and motors.	**Medium:** Uses standard components, precise control.	**High:** Nested structures are difficult to build.
Main Limitations	Large footprint and heavy power requirements.	Low flexibility; trajectory limited by string.	Lack of experimental testing; purely theoretical.

Table 1.1: Summary of the comparison between the selected studies, divided by categories of greatest interest for this work.

challenges of translating the biological system into engineering.
First, all three treat the separation of projection and retraction as a fundamental architectural requirement. This separation is present explicitly in Debray and implicitly in Hatakeyama and Mochiyama through the passive string constraint, while the retraction is absent in Zheng et al. which addresses only projection.
Second, all three rely on a brief, impulsive energy delivery rather than continuous force during ballistic flight, so the end-effector then moves by inertia. This last phase can be conceptualized as the direct engineering analogue of the biological constant-velocity phase described by Wainwright et al. [32] and de Groot [29].
Third, to maximize speed all designs aim to minimize the mass of the moving end-effector and the extendable part.

The approaches diverge substantially in actuation technology and biological fidelity. Debray and Hatakeyama and Mochiyama use respectively electromagnetic and pneumatic impulse generators, both lacking biological counterparts, while only Zheng et al. attempts to replicate the elastic storage structure itself. For retraction, Debray provides the only complete and characterized system; Hatakeyama and Mochiyama use passive elastic constraint; Zheng et al. omits retraction. Even fore this phase of the prey-capure kinematics, none of the three includes a structural analogue of the hyoid bone or entoglossal process.

1.4 Positioning and Aim of the Present Work

The work presented in this thesis shares the biomimetic ambition of the studies reviewed above but differs in its choice of actuation technology, design philosophy, and its explicit treatment of the hyoid–tongue interaction.

Where Debray and Hatakeyama and Mochiyama use electromagnetic or pneumatic impulse generators with no biological analogue, and Zheng et al. employs a rigid mechanical nesting architecture at a biologically unrealistic scale and mass, the present work instead uses a soft pneumatic silicone actuator as the primary active element.
Soft pneumatic actuators offer a functional analogy to the hydrostatic mechanics of the biological accelerator–hyoglossus complex: both deform under distributed internal pressure, both produce a coupled radial–axial deformation, and both are fundamentally compliant and lightweight. At the same time, they are manufacturable using accessible laboratory processes, unlike the high-voltage coilgun circuits and precision electromagnetic components of the reviewed systems.

The design philosophy of this thesis has been guided throughout by three explicit constraints: simplicity of construction, modularity of the actuation architecture, and accessibility of the manufacturing process. The modular architecture, where actuator chambers can be stacked or for future development even independently pressurized, enables stroke and force scaling without redesigning the basic geometry unit, an advantage none of the three reviewed systems currently offers.

The initial design concept for this thesis explicitly included a structural analogue of the hyoid bone, i.e. a rigid central support structure around which the soft actuator is mounted, motivated by the biological question in Sec.1.2.2 whether entoglossal geometry makes a measurable contribution to projection efficiency, apart from the assembly.
This combined hyoid scaffold, serving as both support and launcher together with the soft-actuator system, represents the full scope of the original design intention, and is the first framing in the literature to treat the hyoid bone's mechanical contribution as an explicit experimental question within a robotic context.

However, the work presented in this thesis presents the preliminary design and numerical characterization of the soft actuator component alone (the retractor analogue, which may also function as a protruding element) as a necessary first step toward the complete integrated system.
The hyoid integration and comparative performance testing between the actuator alone and the actuator mounted on the scaffold remain the primary directions for future development.

Chapter 2

Prototype preliminary Design

2.1 Rationale behind the Design Choices

The design choices presented in this work were guided from the outset by two explicit constraints: ease of fabrication and conceptual simplicity. Rather than attempting a systematic comparison across the full breadth of soft robotic possible solutions surveyed in Chapter 1.1, only those solutions compatible with both criteria were retained for further analysis. This initial screening was then followed by a more in-depth phase combining finite element method (FEM) simulations with practical manufacturing considerations that will be later presented in Chapter 4.

The observation of the chameleon's tongue mechanism naturally suggests a bellows-like geometry as the simplest structural form capable of replicating the tongue's extension behaviour. Biologically, this motion corresponds to the unfolding, sock-like release of the accelerator muscle complex from around the entoglossal process; the resulting axial thrust, combined with the elastic energy stored in the intralingual connective tissue sheaths, produces the ballistic projection. A bellows geometry captures the essential kinematic feature of this mechanism: a structure capable of remaining in a compact, pre-loaded configuration and elongating rapidly along its principal axis when actuated, in direct functional analogy to the biological system.

Within this geometric framework, two candidate implementation strategies were identified and evaluated in parallel: a silicone-based pneumatic actuator and an origami-inspired folded structure. Both approaches share the same fundamental operating principle namely axial extension through a controlled change in geometry, but differ substantially in their mechanical behavior, fabrication requirements, and system-level integration. The comparison between the two is discussed in detail in the following section.

2.1.1 Comparison of the Two Design Strategies

The origami approach, and in particular a geometry inspired by the Kresling pattern, was the initial design direction considered. Its primary mechanical appeal lies in the anisotropic stiffness of its folded walls: when properly designed, the panels are rigid in the radial direction while remaining compliant along the axial direction. This is a highly desirable property for a ballistic actuator, because it means that the energy delivered by the pressure source is directed almost exclusively toward axial elongation, with minimal loss to radial expansion. In this sense, an origami structure behaves as a mechanically efficient converter of internal pressure into axial stroke, with an actuation efficiency that approaches the ideal case of a purely uniaxial deformation.
The Kresling pattern further offers an exceptionally high ratio between compressed and extended length, directly analogous to the large stroke-to-rest-length ratio observed during chameleon tongue projection, and its low structural mass is favourable from a dynamic standpoint, as a lighter moving element requires less energy to accelerate.

However, this approach presents several limitations that ultimately led to its exclusion as the primary design direction. First, the fabrication complexity at the prototype scale under consideration is incompatible with the design constraint of accessibility and replicability: the precise fold geometry and the thin-walled construction required for correct kinematic behaviour are difficult to achieve reliably without specialized tooling. Second, origami-based structures are inherently susceptible to fatigue failure at the fold lines under repeated cycling, which limits their durability. Third — and most critically from a system integration perspective — an origami structure is mechanically passive: it can extend when pressurised, but it has no intrinsic retraction capability. Implementing the retraction phase would require a dedicated auxiliary mechanism, such as an elastic restoring element or a separate actuator, significantly increasing system complexity. Finally, the low structural stiffness of origami geometries, which is precisely what makes them lightweight, also means that they cannot independently sustain significant compressive or transverse loads at the end-effector without the addition of a reinforcing structure.

The silicone pneumatic actuator overcomes these limitations but introduces a new challenge. As an isotropic elastomer, silicone lacks the directional stiffness of an origami structure: when pressurized, it expands in all directions, so a significant share of input energy is lost to radial bulging instead of useful axial elongation—an

Feature	**Origami-Based Structure**	**Silicone Pneumatic Actuator**
Fabrication	High complexity: requires precise fold geometry; difficult to replicate without specialized tooling.	Accessible: mouldable using standard laboratory processes; highly repeatable.
Kinematics	Passive/Unidirectional: extends under pressure but lacks intrinsic retraction.	Active/Bidirectional: handles both extension and retraction in a single unit.
Efficiency	High directionality: geometry guides motion without significant energy loss to radial expansion.	Lower (Radial Bulging): isotropic nature causes energy loss; requires shape optimization.
Durability	Limited: susceptible to fatigue failure at the fold lines under repeated cycling.	Stable: chemically stable and reliable, though subject to material hysteresis.
Biomimicry	Low: mechanical behavior is strictly geometric/kinematic.	High: elastic modulus matches biological tissues; stores/releases strain energy.

Table 2.1: Summary comparison between the two possible final design choices.

inefficiency absent from the origami design. To reduce this effect, we optimized the actuator's geometry and wall thickness to maximize the axial-to-radial deformation ratio, the results are presented in 2.2.

Silicone nonetheless offers important advantages. It is easily moulded with standard laboratory methods, chemically stable, and reliably repeatable over many fabrication and actuation cycles, though further fatigue studies are needed because of its hysteresis. Its mechanical behaviour also closely matches that of the biological tissues involved in chameleon tongue projection: the elastic modulus of typical silicone elastomers (10^2–10^3 Pa, depending on formulation) is comparable to that of soft tissues, providing distributed compliance that allows storage of elastic strain energy under pressure and rapid release, analogous to the collagenous sheaths around the accelerator–hyoglossus complex. Unlike the origami option, a sealed silicone chamber is inherently bidirectional: positive pressure causes extension, while vacuum causes retraction, enabling the full projection–retraction cycle with a single actuator and no auxiliary mechanisms. Its intrinsic stiffness also gives sufficient self-support to transmit meaningful forces to the end-effector without extra reinforcement.

Tab. 2.1 summarizes the main advantages and limitations of the two candidate strategies across the criteria most relevant to this application.

On the basis of this comparison, the silicone pneumatic actuator was selected as the primary design strategy for the prototype developed in this thesis. The origami approach and in particular its 3D-printed variant using flexible elastomeric filaments, such as the work done by Melancon et al. [44], which partially mitigates the manual fabrication difficulty while preserving the geometric efficiency, remains a relevant direction for future development, particularly if weight reduction and actuation efficiency become primary performance objectives once the basic architecture has been validated.

2.1.2 Actuation Strategy

Pneumatic actuation was selected as the most appropriate power supply strategy, and its choice is tightly coupled to both the material selection and the performance requirements of the system.

From a practical standpoint, a pneumatic circuit is the simplest actuation system compatible with a soft elastomeric actuator: a pressure source, a control valve, and a sealed chamber are sufficient to generate the complete extension–retraction cycle, without the need for high-voltage electronics, thermally active elements, or complex mechanical transmissions. This directness of implementation is fully consistent with the design philosophy of the thesis.

From a performance point of view, however, the choice of pneumatic actuation is not merely one of convenience — it is the only actuation principle among those reviewed in Chapter 1.1 that simultaneously satisfies all the dynamic requirements of the application. The critical requirement is the ability to deliver a large deformation in an extremely short time interval. When a pressurized supply is rapidly connected to the actuator chamber through a fast-switching valve, the resulting pressure wave propagates through the elastomeric volume at speeds that are orders of magnitude higher than what can be achieved by thermally or electrically driven actuators. Shape memory alloys, for instance, are limited by the rate of heat transfer to and from the alloy, which constrains their actuation bandwidth to frequencies well below 1 Hz in most practical configurations. Dielectric elastomer actuators can in principle operate at higher frequencies, but they require rigid prestraining frames and high-voltage supplies that are incompatible with the compliance and simplicity requirements of this system. By contrast, a pneumatic actuator can transition from rest to full extension in a time interval controlled almost entirely by the valve switching time and the supply pressure, independently of the actuator size or material. This makes pneumatic actuation the only viable candidate for replicating the ballistic acceleration phase of the chameleon tongue, which in the biological system reaches peak accelerations of up to 486 m/s^2 and specific power outputs on the order of 3000 W/kg [35]. The combination of rapid pressure delivery for extension and vacuum application for retraction also reproduces the temporal asymmetry of the biological capture sequence, in which projection is ballistic and nearly instantaneous while retraction is slower and more controlled [35].

2.2 Study of the Unit Cell

The idea is to design a multi-cell actuator body using a specific geometry that can exploit internal pressure to elongate axially while contracting to occupy the smallest possible space in the rest configuration. Different geometries were analysed, also with the aid of FEA software to accelerate the screening process. However, the simulation of a silicone body undergoing large pressure-driven deformations is inherently complex, due to the strong nonlinearities associated with finite strains and hyperelastic material behaviour. For this reason, in this preliminary phase, a full numerical optimisation was not pursued; instead, simplified analytical calculations were used to identify the most promising candidate geometries, which were then compared on a common physical basis.

2.2.1 Geometry Definition

A total of six unit cell geometries were investigated, grouped into three design families. Within each family, variants were obtained by modifying a single geometric parameter, so as to isolate its effect on the actuator's mechanical response.

The choice of a meaningful comparison basis deserves a brief justification. For a pressure-driven soft actuator, the most physically significant fixed parameter would ideally be the internal volume at rest, since at equal initial volume one can directly compare how much axial elongation is obtained for the same amount of injected air, thus obtaining a direct measure of volumetric actuation efficiency. However, controlling the internal volume exactly across geometries of very different shape is impractical in a design phase, and the resulting constraint is not easily interpretable in constructive terms.

A more practical and physically transparent choice is to fix the rest length in the actuation direction h and the maximum outer diameter d, which together define the dimensions of the minimum circumscribed cylinder of the unit cell, as illustrated in Fig. 2.1. This criterion has a clear physical meaning: it compares geometries that occupy the same maximum envelope, which in a real application is typically the first constraint imposed by the available installation space.
The outer diameter d limits the radial footprint of the actuator, while the height h determines how many cells can be stacked in a given axial length. Wall thickness was kept constant at $t = 1mm$ throughout this preliminary study.

The minimum circumscribed cylinder and its defining dimensions are shown in Fig.2.1, and the corresponding values for each geometry are listed in Tab.2.2.

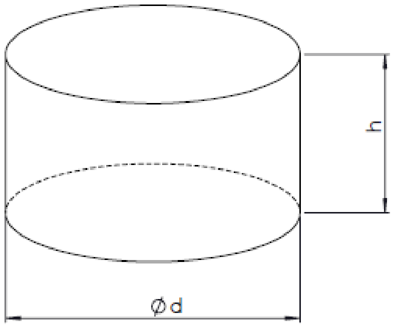

Figure 2.1: unit cilinder, where d is and h is.

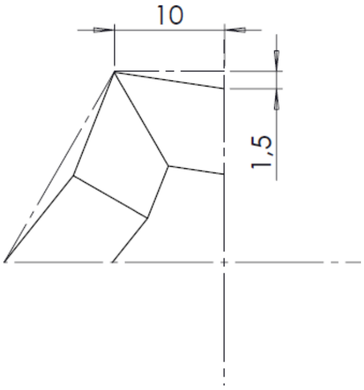

Figure 2.2: Additional geometric dimensions for unit cell model 4.

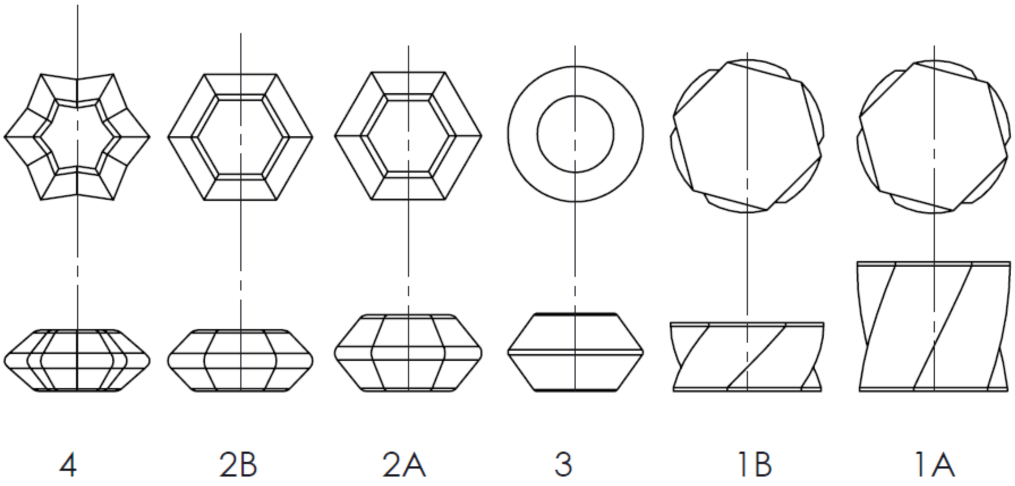

Figure 2.3: Top and front view of the unit cells analyzed.

Models 1A and 1B: Twisted Hexagon

Models 1A and 1A were designed to mimic, at the unit-cell level, the kinematic principle of the chameleon tongue's accelerator muscle. As described in Chapter 1.1, this muscle consists of helically wound fibres around the entoglossal process that

ID	Geometry Description	h [mm]	d [mm]	Sweep Angle
1a	High twisted hexagon	34	40	45°
1b	Low twisted hexagon	18	40	30°
2a	Hexagonal trapezium	20	40	-
2b	Flattened hexagonal trapezium	16	40	-
3	Rounded trapezium	20	40	-
4	Star trapezium	16	40	-

Table 2.2: Geometric parameters for the different actuator design iterations, including height h, diameter d, and sweep angle.

unwind under contraction, driving axial tongue projection. Similarly, the twisted hexagonal unit cell is designed to elongate by untwisting: as internal pressure rises, the sweep angle of the lateral faces approaches zero, converting rotational freedom into axial extension. This coupling between torsion and axial stroke is appealing because it uses the geometric pre-strain of the twisted walls as an additional elastic reservoir, potentially amplifying stroke for a given pressure input.

The two variants differ in their rest height ($h = 34mm$ for 1A, $h = 18mm$ for 1B) and sweep angle (45° and 30° respectively), while the outer diameter is kept constant at $d = 40mm$.

Variant 1A, being taller, has a larger initial sweep angle and more axial length for geometric untwisting, which should produce a larger absolute stroke but also a higher rest volume and stiffer torsional response. The shorter variant 1B, with its smaller sweep angle, should have a softer initial response and smaller stroke, but a higher stroke-to-height ratio, relevant to multi-cell assembly compactness.

Models 2A, 2A, 3, and 4: Trapezoidal Family

Models 2A, 2A, 3, and 4 form a second design family based on a trapezoidal cross-sectional profile. The common operating principle of this family is simple: the inclined lateral faces of each cell act as pressure-loaded ramps. When the internal pressure acts on these inclined surfaces, it generates both a radial and an axial force component. The axial component is what drives elongation; the radial component is responsible for the undesired lateral expansion discussed in Section 2.1. The inclination angle of the lateral faces is therefore the key geometric parameter governing the trade-off between axial force generation and radial bulging.

Models 2A and 3 share a lateral face inclination angle of 125°, measured from the base plane, while models 2B and 4 adopt an angle of 130°. The influence of increasing the inclination angle, that is, of rendering the lateral faces steeper with respect to the axis, can be explained with a simple pressure decomposition, which will be carried out in a more rigorous manner in the subsequent section.

However, a steeper face also implies a smaller internal volume for the same outer diameter and height, since the trapezoidal profile becomes more slender. A smaller internal volume means less air capacity per cell and, in a multi-cell assembly, a larger number of cells is required to achieve a given total stroke, increasing fabrication complexity and the number of inter-cell sealing interfaces.

This trade-off between face inclination, internal volume, and system-level complexity was explicitly acknowledged in the design process, and a more rigorous resolution through formal optimization methods is identified as a priority direction for future work.

Model 3 is the only geometry in the family with fully rounded lateral surfaces, free of geometric edges. It was included as a baseline to assess the effect of surface continuity on the deformation behaviour: a smooth surface distributes stress more uniformly, reducing stress concentrations at re-entrant corners and potentially improving fatigue life. However, the absence of edges also means the absence of any local bending stiffness concentration, which, as discussed below, is disadvantageous to radial stiffness.

Model 2A was developed as a direct evolution of model 3, based on the observation that sharp edges in the cross-section locally increase wall bending stiffness. Where walls meet at a sharp angle, they act as folded plates, which are much stiffer perpendicular to the fold than flat or smoothly curved panels of the same thickness. This radial stiffening limits outward bulging under pressure and directs more internal pressure work into axial elongation—exactly the efficiency gain needed to offset the isotropic compliance of silicone identified in Section 2.1.

Model 4 further develops this logic by alternating inward and outward pointing vertices in a star shaped cross-section. The re-entrant geometry forms a circumferential network of fold lines, maximising local stiffening features per unit perimeter and giving the highest radial rigidity of all geometries.
However, model 4 was rejected mainly for fabrication reasons: the alternating concave and convex features greatly complicate mould design and especially demoulding, and the narrow inward-pointing tips are prone to incomplete silicone filling, causing defects.

2.2.2 Simplified Analytical Model

In order to compare the six candidate geometries on a physically consistent basis, a simplified analytical framework was developed. Given the geometric and material complexity of the problem (large deformations, hyperelastic material, and coupled axial and radial response) no attempt was made to derive a closed-form solution for the full deformation field. Instead, two complementary first-order estimates were sought for each geometry: the axial force output and the tendency toward radial expansion. Together, these two quantities allow a qualitative ranking of the geometries in terms of actuation efficiency.

The axial force generated by a pressurized unit cell was estimated using the principle of virtual work.
Consider a unit cell at internal gauge pressure p, in a configuration characterized by height h. If the cell undergoes a virtual axial displacement δu, the internal volume changes by δV. The work done by the pressure on this virtual displacement must equal the work done against the external axial load F_{ax}:

$$p \cdot \delta V = F_{\text{ax}} \cdot \delta u \tag{2.1}$$

From which the axial force can be expressed as:

$$F_{\text{ax}} = p \frac{\partial V}{\partial h} \tag{2.2}$$

This result has a transparent physical interpretation: the axial force output of the actuator is directly proportional to the rate of change of internal volume with axial displacement, i.e. to the *axial volumetric sensitivity* of the cell geometry. A geometry that produces a large increase in internal volume for a small axial extension generates a high axial force at a given pressure. This formulation is particularly convenient because $\partial V/\partial h$ can be computed analytically from the cell geometry without solving for the stress field, and it provides a single scalar metric for ranking the geometries independently of the material model.

For each geometry, $\partial V/\partial h$ was evaluated analytically by expressing the internal volume under the assumption of rigid walls. This simplification overestimates the true force output but provides a consistent upper bound for comparison purposes. The assumption is more accurate for geometries with stiffer walls (models 2B and 4) and less so for the rounded model 3, where wall compliance plays a greater role.

The tendency of each geometry to expand radially was assessed through a simple force decomposition on the inclined lateral faces. For a planar face of area A inclined at angle α with respect to the horizontal (base) plane, the internal pressure p produces a resultant force $F = p \cdot A$, normal to the face. This resultant can be decomposed into an axial component and a radial component, namely:

$$F_{\mathrm{ax}} = pA \sin\alpha \qquad \textit{and} \qquad F_{\mathrm{rad}} = pA \cos\alpha \tag{2.3}$$

The ratio $F_{\mathrm{ax}}/F_{\mathrm{rad}} = \tan\alpha$ therefore provides a direct measure of the geometric efficiency of each inclined face in converting internal pressure into useful axial force. Steeper faces (larger α) yield a more favourable ratio. For the trapezoidal family, this ratio was computed for the two inclination angles considered, confirming that the more steeply inclined variants (2a and 3) produce a higher axial-to-radial force ratio. However, as noted in Section 2.2.1, the steeper inclination also reduces the internal volume, which partially offsets the efficiency gain in terms of absolute force output per cell.

For the twisted geometries (1A and 1B), the faces are not planar and their orientation varies continuously along the height; an equivalent inclination angle was estimated by linearising the face geometry at mid-height, which provides a first-order approximation sufficient for the purposes of this comparative analysis.

Effect of Geometric Edges on Radial Stiffness

The radial stiffness of each geometry cannot be captured by the pressure decomposition alone, since it depends on the bending stiffness of the wall rather than on the pressure resultant. A thin-walled panel of thickness t, width b, and elastic modulus E has a bending stiffness that scales as $(E \cdot t^3)/b^2$ in its weakest direction. A flat or smoothly curved panel offers no geometric amplification of this stiffness. By contrast, a panel that meets another at a corner angle θ behaves locally as a folded plate, whose effective radial stiffness is significantly higher than that of a flat panel of the same thickness, due to the geometric constraint imposed by the fold line.

This argument provides the physical justification for the progression from model 3 (smooth, no edges) to model 2A (hexagonal edges) to model 4 (star-shaped, alternating edges): each step increases the number and sharpness of fold lines per unit perimeter, progressively raising the radial stiffness of the cell wall. A higher radial stiffness reduces F_{rad}, responsible to induce bulging, redirecting a greater fraction of the pressure work into axial elongation. The penalty, as discussed in Section 2.2.1, is increased fabrication complexity and, in the limit of model 4, the introduction of stress concentrations at the re-entrant tips that may limit fatigue life.

2.2.3 Summary and Geometry Selection

The analytical framework described above does not yield quantitative predictions of stroke or force with engineering accuracy. However, it provides a physically grounded basis for ranking the geometries and narrowing the candidate set before

committing to full numerical simulation. The key metrics derived from the simplified model are summarized qualitatively in Tab. 2.3.
On the basis of the analysis, model 2A emerges as the most balanced candidate.

Model	$\partial V/\partial h$	F_{ax}/F_{rad} **ratio**	**Radial stiffness**	**Overall ranking**
1a	High	Moderate	Low	Moderate
1b	Moderate	Moderate	Low	Moderate
2a	High	High	Moderate	High
2b	Moderate	Moderate	Moderate	Moderate
3	High	High	Low	Moderate
4	Moderate	Moderate	High	Moderate

Table 2.3: Qualitative summary of the simplified analytical quantities for each unit cell geometry. $\partial V/\partial h$ represents the axial volumetric sensitivity; F_{ax}/F_{rad} is the axial-to-radial force ratio; radial stiffness reflects the geometric bending stiffness contribution of edges and fold lines.

Models 1A and 1B present an interesting kinematic concept but their analytical characterization is more complex, and their radial stiffness is inherently low due to the absence of fold lines in the cross-section. Model 4, while mechanically attractive for its radial rigidity, was excluded on fabrication grounds as discussed previously. Model 2B was retained as a secondary candidate alongside 2A, to allow a direct experimental comparison of the effect of face inclination angle under otherwise identical conditions.

Chapter 3

Hyperelastic Material Characterization, Modeling and FEA Prediction Accuracy

When talking about SPAs, silicone rubbers and elastomers are quite often the prediliged materials; popular examples in this sense are Ecoflex from SmoothOn, Elastosil from Wacker Chemie AG and Sylgard from Down Chemicals [3], which are more commonly used in mold-making and special effects industries but still very versatile also for other applications.

These types of materials can easily provide a high power-to-weight ratio, which is a main characteristic for devices designed to interact with biological organisms or fragile objects without causing damage.
In this specific design, the properties of the Ecoflex were also very useful in the back-drivability of the model, as well as the flexibility of the design and production techniques that do not require complex machinery.
Typical biomaterials in living organisms, particularly those associated with muscle tissues and fat, tend to deform elastically when a force is applied. This is why in soft robotics many "soft" material used are viscoelastic. These classes of materials exhibit time-dependent mechanical properties that can be characterized by their storage and loss moduli, which quantify, respectively, the elastic and viscous components of their response. This viscoelastic behavior enables them to dissipate energy and maintain stability under dynamic loading. On the contrary, purely elastic materials (e.g., wood, bone, steel) do not dissipate energy when subjected to dynamic loads, and their mechanical response can be fully described by the storage

modulus alone.

For this work, The Ecoflex 00-30 from SmoothOn was selected, considering that it is widely used in soft robotics, allowing for easy comparison. Among the other properties, it also exhibits a very high percentage of elongation at break (900%) and 45 minutes pot life [45] .

Hyperelasticity is commonly used to predict the behavior of different elastomer-like materials, mainly due to its straightforward implementation and its availability in virtually all FEA software packages [46].
To develop a reliable numerical model of the prototype, it is necessary to use data that accurately represent the actual behavior of the selected material, with particular attention to the specific manufacturing processes adopted in this work. To this aim, a dedicated experimental campaign was carried out. On the basis of the resulting stress–strain curves, a suitable constitutive model was then selected and its parameters were calibrated. Finally, the calibrated material model was implemented in the finite element model, in order to verify the accuracy and predictive capability of the numerical results.

3.1 Experimental data extrapolation

The material used to make the actuator was subjected to uniaxial tesile tests according to ASTM D638 (Type IV) with the aim of an INSTRON 3368 testing machine, working at a rate of 500 mm/min to obtain accurate material properties. The testing fixture used had a maximum load capacity of 1 kN (Fig. 3.6); consequently, the recorded curves exhibit slight oscillations, particularly at the beginning of the test.

3.1.1 Manufacturing

The samples were produced by casting the silicon into a 3D printed mold, the design of which is shown in Fig. 3.1, according to the dimensions specified in the standard and illustrated in Fig. 3.2
To minimize the presence of air bubbles generated during mixing of the bi-component material, several strategies were tried. The most effective approach consisted of allowing the silicone to rest for approximately 10–15 minutes, after it was poured into the mold, before sealing it. This waiting time was sufficient to allow most of the entrapped air bubbles to rise to the free surface, resulting in a substantially bubble-free bulk material. Nevertheless, complete elimination of bubbles could not be achieved.

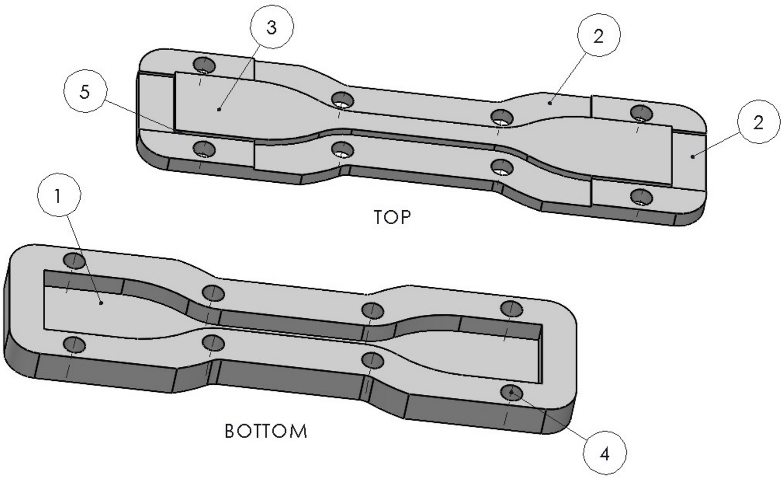

Figure 3.1: Technical specifications of the mold for sample fabrication. During the fabrication process, the silicone material was poured into the main cavity(1). Then, the top part was flipped and compressed over the bottom letting the excess material to overflow through the lateral channels (2). Finally, the two parts were clamped together through the clamping holes (4). The upper wall (3) has a thickness of 1 mm (5) to facilitate the discharge of excess material and ensure the desired specimen thickness

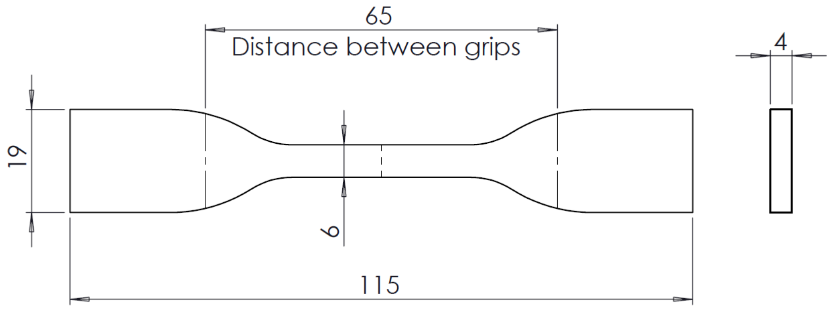

Figure 3.2: Specimen main dimentions (ASTM-D638 Type IV)

3.1.2 Testing procedure

Each specimen was placed in the grips of the testing machine, taking care to align the long axis of the specimen and the grips with an imaginary line that joins the points of attachment of the grips to the machine [47]. Despite the grips being tightened uniformly and securely, slippage of the specimen occurred in the first

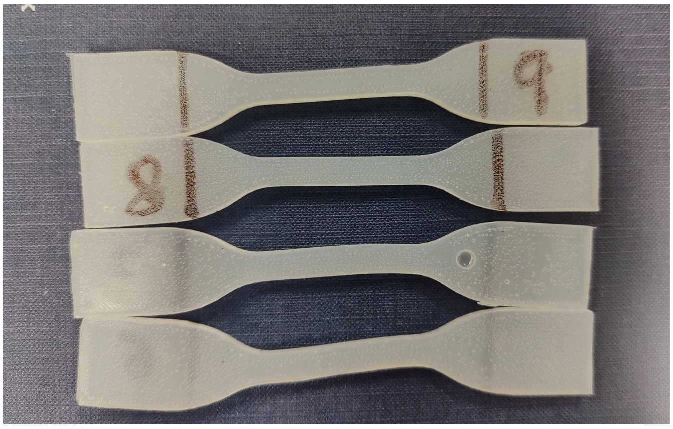

Figure 3.3: Some of the samples. It is slightly visible that the surface of the samples close to the top part of the mold shows some small air bubble. One of the samples even shows a bubble of important size that in this case, observing the curve obtained and the behavior during the loading, it's possible to assume it did not affected the results of the test.

batch of samples, which was therefore excluded from further analysis. A technique that has been found useful in this sense was interposing thin two sided abrasive paper sheets between the clamped surfaces of the specimen and the grip surfaces of the fixtures.This modification substantially improved the test performance but was still insufficient to completely eliminate the slippage issue. Nevertheless, the tests conducted were considered acceptable and a total of ten samples were tested using this measure.

During post-processing, sample 1 exhibited a clear deviation from the expected behavior, likely due to vibration in the testing environment. Consequently, this specimen was excluded from the dataset used for the following calculations. In Fig. 3.4, the raw data acquired during the tests are presented, with sample 1 removed.

In Fig. 3.5 the percent tensile strain was computed as follows:

$$\epsilon_{\%} = \frac{\Delta L}{L_0} * 100 = \frac{(L - L_0)}{L_0} * 100 \tag{3.1}$$

where ΔL is the increment of distance between gauge marks and it was recorded directly from the Instron data acquisition software, after setting to zero the initial elongation at the beginning of each test; L_0 is the original distance between gauge marks and is equal to 25 mm for each sample.
The tensile stress is:

$$\sigma = F/A_0 \tag{3.2}$$

F is the force vector recorded from the test and A_0 is the initial value of the cross-sectional area of each sample, measured with the procedure presented in the

next section.
Assuming that the volume of the test specimen does not change during the test, it's also possible to compute the true tensile stress can be computed as:

$$\sigma_T = \sigma(1+\epsilon) = \sigma L/L_0 \tag{3.3}$$

where, in this case, ϵ is the tensile strength and not its percent value.

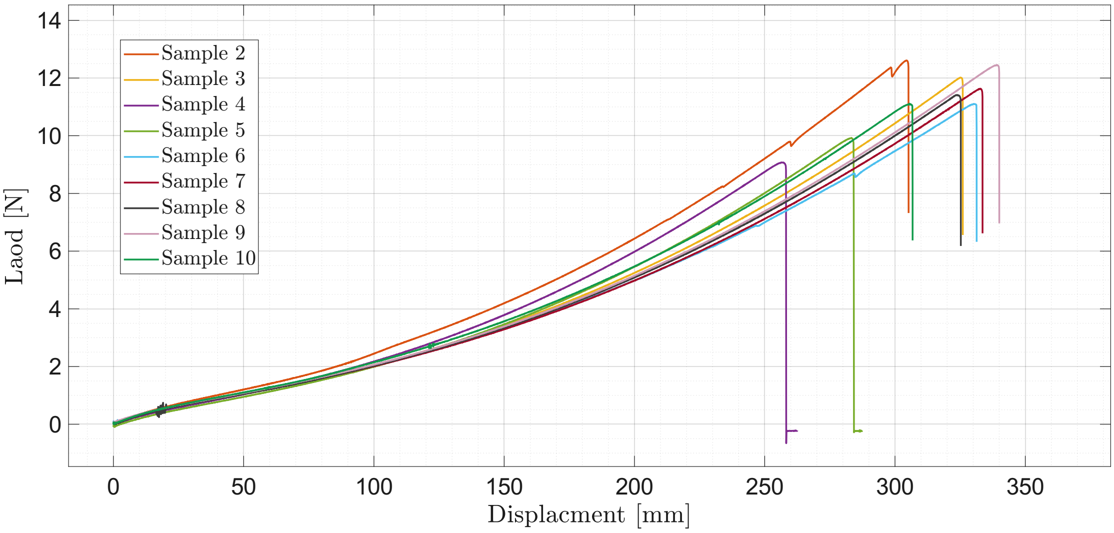

Figure 3.4: Raw Displacement-Force curves. Sample 8 (in black) shows a vibration at the beginning of the test due to the operator, who absentmindedly leaned on the work table; this in any case does not affect the validity of the test, which clearly continues with fully regular behavior. The small steps shown in the curves from Sample 2 and Sample 6 can be explained taking into account a small slippage of the sample that can be considered acceptable as it's clear from the results that below a certain limit it does not affect the overall behavior of the curve but may have affected the break of the sample.

3.1.3 Calculation

In this section the calculations employed are reported and the obtained results are presented in summary in Table 3.1.

For each sample, the cross section was determined by multiplying the mean width and thickness of the specimen, obtained from three independent measurements.Tensile strength was determined for each sample considering the respective maximum applied load and the corresponding cross-sectional area, as previously described; the final value reported in Tab. 3.1 was therefore obtained as the arithmetic mean calculated across all nine specimens. For the calculation of the

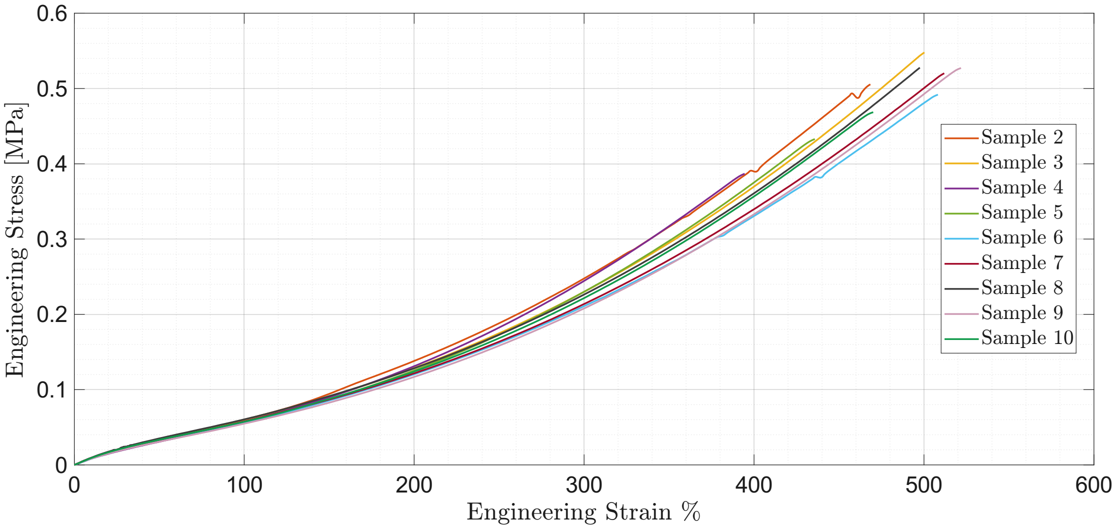

Figure 3.5: Stress–strain curves after application of noise reduction, truncated before the failure.

percent elongation at break, the same procedure was followed.
The true tensile stress at break is also reported in Tab. 3.1 for the sake of completeness.

The 100% Modulus represents the elastic modulus at 100% strain (i.e. $\epsilon = 1$) and was extracted directly from each of the experimental curves and here reported as the arithmetic mean. For each quantity, the standard deviation was calculated as follows:

$$s = \sqrt{\frac{\sum(x - \bar{x})^2}{n - 1}} \tag{3.4}$$

where s is the estimated standard deviation, x is the value of the single observation, n is the number of observations, and $\bar{x}$ is the arithmetic mean of the set.

Property	Value [MPa]	Value [psi]	Value [%]
Tensile strength at break	0.490 ± 0.053	71.09 ± 7.67	–
True tensile stress at break	2.365 ± 0.427	342.96 ± 61.89	–
100% Modulus	0.058 ± 0.002	8.41 ± 0.28	–
Percent elongation at break	–	–	480.02 ± 44.15

Table 3.1: Main characteristics of Ecoflex 00-30 obtained from tensile tests (ASTM-D638). All the values are to be inteded as arithmetic means calculated across the samples batch.

Compared to the values reported in the material's technical datasheet, differences

Figure 3.6: Experimental setup, detail of the 1kN fixture.

are observed especially in terms of the percent elongation at break, which, in the experimental evaluation, was found to be substantially lower, attaining 480% as opposed to the 900% reported in the technical data sheet (TDS). However, the 100% Modulus results are very close to the expected ones, with a difference of 1.59 psi only.

The discrepancy between the 100% Modulus consistency and the collapse in elongation can be explained by the fact that the manufacturing process did not completely eliminate air bubbles in the samples which, although small in size, were nonetheless homogeneously dispersed within the material. The results show that the existing defects do not so much affect the intrinsic stiffness of the matrix as act as stress concentrators. While in the early stages of deformation the material responds elastically and in line with the TDS, as the deformation increases the voids become critical initiation points for crack propagation, leading to premature structural failure well before the theoretical limit is reached.

As this class of materials is known to be strongly rate-dependent and highly sensitive to the speed at which the load is applied, it is also important to note that the

a b

Figure 3.7: (a) Representative specimen at the onset of testing and (b) at a stage near the end of the experiment. These images clearly demonstrate the pronounced elongation, which is characteristic of the mechanical response of this material.

discrepancy in the results may also have been influenced by the dissimilarity in the loading rate that have been adopted.

3.2 Isotropic Hyperelasticity models

To investigate the material behavior using an analytical approach, it is first necessary to select an appropriate constitutive model and subsequently determine the corresponding material parameters by calibrating the model against acquired experimental data.

With the advent of new plastic materials and the increased use of them in research and commercial fields, it became necessary to create an analytical model that would appropriately describe their behavior. From the experimental observations of the stress–strain response of rubber materials was sufficiently evident that the linear theory of elasticity—particularly Hooke's law, which has been in use since the 17th century—was inadequate for characterizing the mechanical behaviour of such materials. Consequently, to analyse materials with nonlinear mechanical properties, which typically exhibit large deformations under relatively small applied stresses, a nonlinear extension of classical elasticity theory was developed, firstly by Mooney [48] and Rivlin [49]. This nonlinear elasticity framework, employs a strain-energy function W to describe the mechanical behaviour of these materials in energetic terms.

It is important to note that hyperelastic material models are generally straightforward to implement and calibrate and are computationally efficient; however, they do not account for hysteresis effects under cyclic loading, nor do they incorporate rate-dependent behavior or viscoelasticity.

For the materials analyzed in this work, both the silicone and the musclular tissue, the hypothesis of isotropy and incompressibility can be made [50], helping the simplification of both the experimental testing and the procedure of the analytical model selection. In this case, it is in fact demonstrated being sufficient to test the material with uniaxial loading only [51]. As a general guideline, hyperelastic models that do not depend on $I2$ (*second strain invariant*) usually need fewer experimental tests [46]. This is because, in such cases, the free energy function reduces to a scalar function of a single variable ($I1$, *first strain invariant*), and this dependence can be completely characterized using just one experiment.

Note that to verify the accuracy of a model it is recommended to carry out experimental tests in several loading modes, which is something that could definitely be done to confirm the validity and robustness of this work's results.

Three different models have been selected from the literature, deemed the most appropriate for the specific focus of the present study. In the following section, these models are calibrated using the experimental dataset, and the quality of the resulting fits is evaluated and compared in order to identify the model that provides the smallest error.

3.2.1 Strain-Energy Function (W)

The Strain energy function, or *Helmholtz free energy*, is the variable that represents the energy stored in a material per unit of reference volume as a function of strain. This function is obtained from symmetry, thermodynamic and energetic considerations. If the material is isotropic, the strain-energy function can be written as follows:

$$W = f(I_1, I_2, I_3) \tag{3.5}$$

where

$$I_1 = \sum_{i=1}^{3} \lambda_i^2$$

$$I_2 = \sum_{i,j=1}^{3} \lambda_i^2 \lambda_j^2, \quad i \neq j \tag{3.6}$$

$$I_3 = \prod_{i=1}^{3} \lambda_i^2$$

being λ_1,λ_2 and λ_3, the principal stretches. When hyperelastic materials are assumed to be incompressible, then $I3 = 1$; as a result, only two independent strain invariants remain, namely $I1$ and $I2$. Consequently, the strain-energy function W depends solely on $I1$ and $I2$. As strain invariants depend on principal stretches, the strain-energy functions may also appear as a function of the stretches:

$$W = W(\lambda_1, \lambda_2, \lambda_3) \tag{3.7}$$

Therefore, the different constitutive models formulated to describe the mechanical response of these materials differ in the equation that links the strain energy function to the three Cauchy invariants or, equivalently, to the three principal stretches. The various approaches adopt different levels of complexity, for example by making W depend on both invariants (e.g. Mooney–Rivlin) or only on one of them (Yeoh [52], Neo-Hookean). For a more in-depth treatment of the subject, the reader is referred to [46], [53] and, more specifically related to this work, [54].

3.2.2 Principal Cauchy stresses as function of λ_i and I_i

As stated by Holzapfel [53], for an isotropic hyperelastic material, it can be written with generality that each principal Cauchy stress is:

$$\sigma_i = J^{-1} \lambda_i \frac{\partial W}{\partial \lambda_i}, \quad i = 1, 2, 3 \tag{3.8}$$

Applying Eq. 3.8 to an incompressible material, the previous equation now becomes:

$$\sigma_i = \lambda_i \frac{\partial W}{\partial \lambda_i} + p, \quad i = 1, 2, 3 \tag{3.9}$$

Where the volume ratio is $J = 1$, due to the incompressibility condition, and p represents the hydrostatic pressure. The value of the latter can be obtained applying the boundary conditions that, for an uniaxial tension load case, are:

$$\sigma_2 = \sigma_3 = 0 \tag{3.10}$$

eventually leading to the equation:

$$\sigma_1 = \lambda_1 \frac{\partial W}{\partial \lambda_1} - \lambda_3 \frac{\partial W}{\partial \lambda_3} \tag{3.11}$$

It is also advantageous to reformulate the same equations by expressing the stress components in terms of the invariants, thereby explicitly highlighting the dependence of the strain-energy functions on these invariants. This, in turn, results in a more compact formulation of the stress–strain relationship. This alternative representation is particularly advantageous for the constitutive models adopted in the present study.
Adopting the same assumptions as before ($J = 1$ and uniaxial tension as in Eq. 3.10, the final expression is:

$$\sigma = 2\left(\lambda^2 - \frac{1}{\lambda}\right)\left(\frac{\partial W}{\partial I_1} + \frac{1}{\lambda}\frac{\partial W}{\partial I_2}\right) \tag{3.12}$$

Where λ is computed as:

$$\lambda = 1 + \epsilon \tag{3.13}$$

being ϵ the engineering tensile strain.

To derive the analytical expression for uniaxial tension under a specific constitutive model, the strain energy function of each material model must be replaced in the Eq.3.12 or 3.11 by the specific functional form corresponding to the material model under consideration.

3.2.3 Neo-Hookian Model

In this model the strain energy function is assumed to be dependent only to the first invariant.

$$W_{Hookean} = c_1(I_1 - 3) \tag{3.14}$$

Therefore, the experimental data can be modeled fitting only one constant parameter, i.e. c_1. Moreover, the constant parameter allows us to know the shear modulus by the relation $\mu = 2c_1$. The NH model is valuable because of its simplicity—once the shear modulus is known, the material response under any loading condition can be computed reliably and with high computational efficiency. However, its primary drawback is that it only provides accurate predictions over a relatively narrow range of conditions.

With Neo-Hookean (NH) model assumptions, the Cauchy stress equation becomes:

$$\sigma_{Hookean} = 2c_1 \left(\lambda^2 - \frac{1}{\lambda} \right) = \mu \left(\lambda^2 - \frac{1}{\lambda} \right) \tag{3.15}$$

3.2.4 Mooney-Rivlin Model

The Mooney-Rivlin (MR) model is an extension of the NH model that attempts to improve the accuracy by including a linear dependence on the second invariant I_2. The Helmholtz free energy function in the MR model is expressed by:

$$W_{Mooney-Rivlin} = \sum_{i=1}^{3} c_i (I_i - 3) \tag{3.16}$$

Using Equation 3.12 it can be shown that the Cauchy stress for the MR model is given by:

$$\sigma_{Mooney-Rivlin} = 2 \left(\lambda^2 - \frac{1}{\lambda} \right) \left(c_1 + c_2 \frac{1}{\lambda} \right) \tag{3.17}$$

It is important to note that the MR model, which is characterized by two constant parameters, c_1 and c_2, can be an improvement to the predictive capability of the NH model. However, it may exhibit instability when a negative value of c_2, calibrated to fit a specific load case, is employed to simulate a different loading condition.

3.2.5 Yeoh Model

The Yeoh Model [52] is based on a strain-energy function depending only on the first strain invariant through a third-order polynomial, with no dependence on I_2. Because it includes higher-order I_1 terms, this model can yield more accurate predictions than the NH model, while at the same time potentially avoiding some of the stability problems associated with the Mooney–Rivlin model [46].
Here, the strain-energy function can be expressed as:

$$W_{Yeoh} = \sum_{i=1}^{3} c_i (I_1 - 3)^i \tag{3.18}$$

where c_1, c_2 and c_3 are the constant parameters resulting form the experimental data fitting.

The stress is consequently evaluated using:

$$\sigma_{Yeoh} = 2\left(\lambda^2 - \frac{1}{\lambda}\right)\left(c_1 + 2c_2(I_1 - 3) + 3c_3(I_1 - 3)^2\right) \tag{3.19}$$

3.3 Material Parameters Calibration Procedure

In this section, the curve-fitting procedure is described step by step. The process encompasses the preparation of the experimental data, the computation of the principal physical quantities as previously outlined, and, finally, the algorithm employed for the extraction of the constant coefficients.

The most challenging aspect of this procedure is to find a good initial guess of the material parameters, in order to ensure that the solution obtained by the minimization algorithm is close to the global optimum. An inadequate initial guess can trap the algorithm to an undesired local minimum and can also significantly increase the computational cost and duration of the process. A common approach in this sense is to use a Monte Carlo statistical method [55], that allows to restrict the range of research to a pre-defined interval.

For the purposes of this study, the initial coefficients were most conveniently specified by adopting values reported in previous publications on the same kind of materials as Ecoflex and same material models and possibly updating these values with the results generated during the first iteration, if the obtained outcome is considered unsatisfactory, following the workflow as in Fig. 3.8. This strategy was eventually found to be sufficiently reliable, looking at the fitting results. The values of initial guesse of the constant parameters are reported in Tab. 3.2.

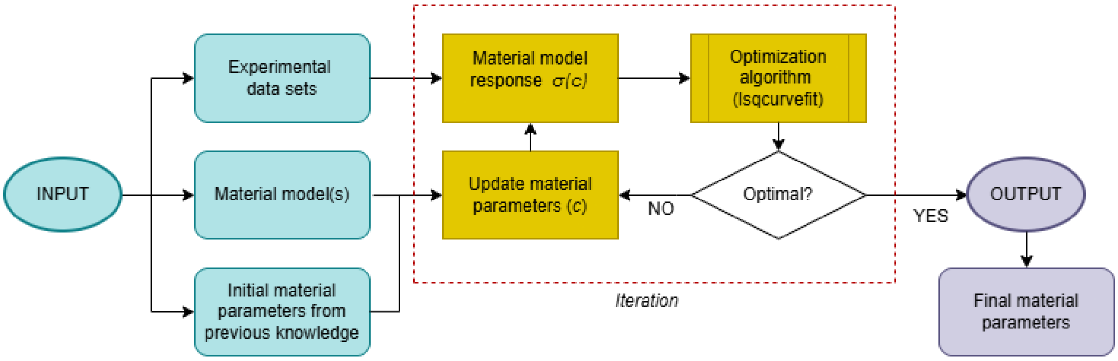

Figure 3.8: The procedure of curve-fitting method to identify the parameters of a hyperelastic material model.

Finally, it is important to note that the entire data extraction procedure (and in particular the constitutive material models' equations) is based on the definition of true stress given in Eq. 3.3, rather than on engineering stress. The main difference between these two measures is that the former accounts for the reduction in the cross-sectional area of the specimen during the test—an effect that cannot be considered negligible for a hyperelastic material such as Ecoflex 00-30, given the large elongations it exibits; whereas the latter is computed under the assumption of a constant cross-sectional area, equal to the value measured under unloaded conditions prior to testing.

Model	$c_{0,1}$ [MPa]	$c_{0,2}$ [MPa]	$c_{0,3}$ [MPa]
Neo-Hookian	0.01	-	-
Mooney-Rivlin	0.02	0.01	-
Yeoh	0.005	0	0

Table 3.2: Inital guesses of the material constant parameters for each material model

3.3.1 Experimental Data Preparation

For each specimen, the maximum load was first identified, and the corresponding segment of the data vector beyond this peak was removed. This procedure ensured that only the mechanically meaningful portion of the load–response curve was retained, thereby preventing the post-failure behavior recorded by the testing machine from influencing the fitting results.

As described in Section 3.1, a 1 kN load cell was employed for the tests, which introduced a certain level of noise into the recorded data. To attenuate this noise and prevent it from affecting the determination of the coefficients, the `smoothdata` algorithm [56] was applied on both stress and strain/elongation vectors (the results are show in Fig. 3.5. Specifically, the `sgolay` option, corresponding to the Savitzky–Golay filter, was selected. This filter performs smoothing by fitting a quadratic polynomial within a moving window of 50 samples. Such an approach can be more effective than alternative smoothing techniques, particularly when the signal exhibits rapid variations.

3.3.2 Curve Fitting

Before running the fitting code and after the definition of λ and σ_T, each constitutive model is implemented on matlab as a function, following the equations as in Sec. 3.2.4, 3.2.3 and 3.2.5.

Then, it was chosen as fitting alorithm the `lsqcurvefit` [57] already implemented in Matlab. It is a nonlinear least-square solver that find the coefficients c that solve the problem:

$$\min_c \|F(c,\lambda) - \sigma_T\|_2^2 = \min_x \sum_i (F(c,\lambda_i) - \sigma_{T,i})^2 \tag{3.20}$$

where $F(c,\lambda)$ has a different form for each material model taken into account.
To take into account the contribution of each specimen, all the values of λ and σ_T were collected into single vectors, which serve as the reference point for the fitting algorithm.

The true stress–stretch response was determined numerically on the basis of the calibrated hyperelastic constitutive models; see Fig. 3.9 for the results.

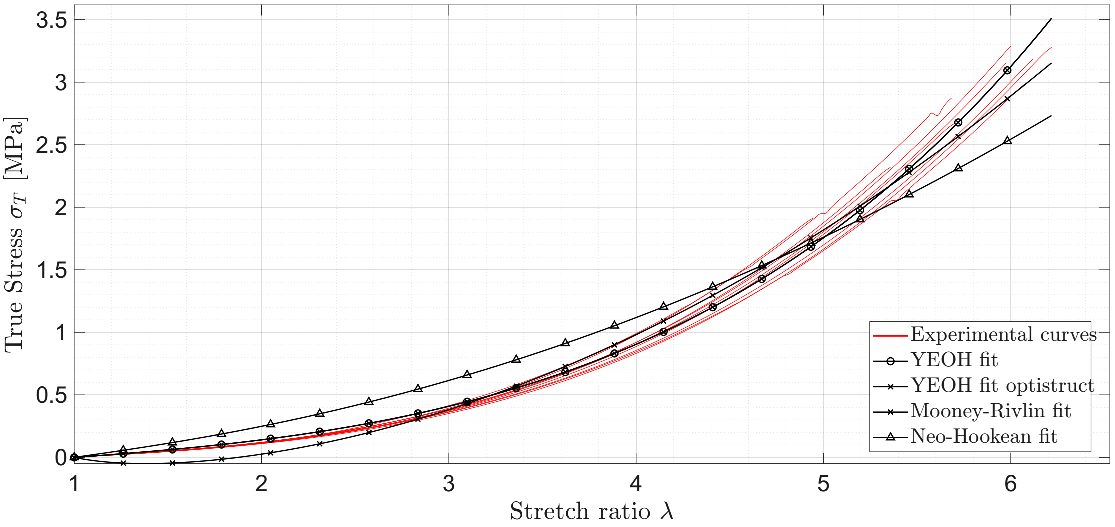

Figure 3.9: Comparison of the different hyperelastic models' prediction with the nine laboratory test results.

The Tab. 3.3 lists the parameters that were determined by fitting the phenomenologica material models Neo-Hookian, Mooney-Riviling and Yeoh.
To qualify the accuracy of the different material models the coefficient of determination (COD) R^2 was used, which is evaluated as:

$$R^2 = 1 - \frac{\sum(\sigma_{i,\mathrm{p}} - \sigma_{i,\mathrm{e}})^2}{\sum(\sigma_{i,\mathrm{p}} - \bar{\sigma}_{\mathrm{e}})^2} \tag{3.21}$$

where the subscript $(.)_p$ stands for predicted, $(.)_e$ for experimental and $\bar{\sigma}$ is the mean value of the stress.
As an additional metric to qualify the accuracy and compare the performance of the different material models, the root mean square error (RMSE) can be employed. This parameter conveys the same concept as the COD, R^2, but is expressed in

Hyperelastic Model	Material Parameters	Number of Iterations $\epsilon = 1.0 \times 10^-6$	R^2	RMSE
Neo-Hookean	$c_1 = 0.0355$ (MPa)	13	0.9400	0.2056 (MPa)
Mooney-Rivlin	$c_1 = 0.0586$ (MPa) $c_2 = -0.1099$ (MPa)	2	0.9875	0.0937 (MPa)
Yeoh	$c_1 = 0.0186$ (MPa) $c_2 = 4 \times 10^{-04}$ (MPa) $c_3 = 2.3 \times 10^{-14}$ (MPa)	2	0.9924	0.0732(MPa)

Table 3.3: Hyperelastic material parameters found by the curve fitting method.

physical units rather than in purely statistical terms. The corresponding values are reported in Tab. 3.3 and are computed as:

$$RMSE = \sqrt{\frac{E}{n}} \tag{3.22}$$

where E is once again the fitting error and n is the number of experimental points of the experimental stress vector.

As it is shown in Tab.3.3, the most accurate fit for this specific data set is represented by the Yeoh material model, having the higher COD, the lower error and a very low RMSE, which means minimal physical error. The difference between the RMSE of the Neo-Hookean model (0.2056 MPa) and that of the Yeoh model (0.0732 MPa) shows that the Yeoh model is more than twice as accurate.

3.4 Finite Element Modeling

To verify the validity of the obtained results, a final verification step was carried out by developing a finite element model (FEM) of the same specimen illustrated in Fig. 3.2, integrating into the simulation the material parameters identified from the experimental tests.

In addition to enabling validation of the adopted constitutive law and permitting reasonably accurate simulation of the material response under alternative loading conditions—such as compression or torsion—without the need for an extensive and costly experimental campaign, the development of a finite element model provides the further substantial advantage of yielding more precise and reliable predictions when integrated into FEM analyses of the complete prototype. This, in turn, significantly accelerates the overall prototyping process. The numerical model was developed using the Altair HyperMesh pre-processor in combination with the OptiStruct solver.

3.4.1 Mesh creation

Initially, the CAD model of the manufactured specimen was imported into the finite element analysis software. A two-dimensional mesh was generated on the main surface of this geometry. Given that the minimum characteristic dimension of the geometry to be meshed was 6 mm, a target element size of 1 mm was selected for the individual elements.
In this stage, the mesh quality was evaluated using the `qualiyindex` command.

After the two-dimensional mesh on the main face was created, a three-dimensional solid mesh consisting of CHEXA and CPENTA elements was generated from the planar mesh. This was performed by applying the `linedrag` command along the `(-)z axis` over a distance of 4 mm, corresponding to the specimen thickness. Four elements were created along the z-direction, resulting in a total of 6560 elements, as illustrated in Figure 3.10.

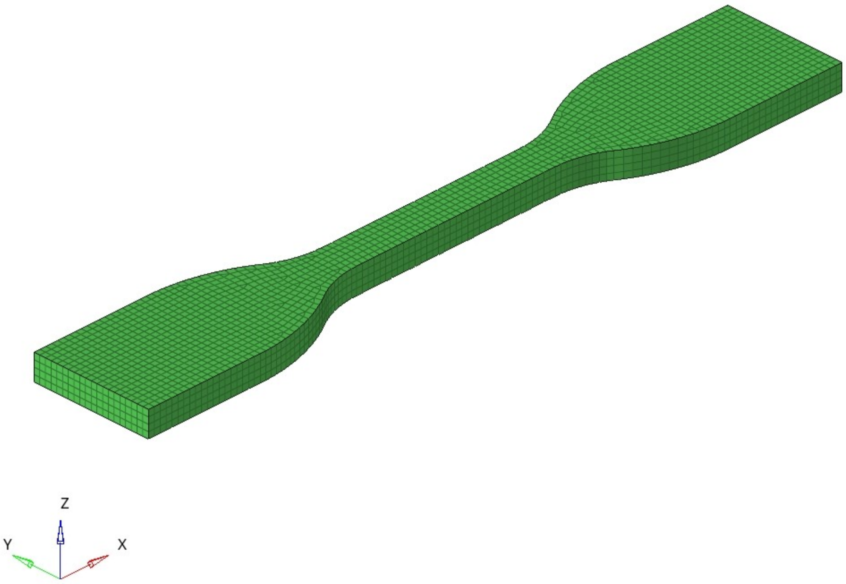

Figure 3.10: Solid Mesh distrubution and quality on sample

3.4.2 Boundary Conditions

Imposed Displacement

A RBE3 element was created to simulate the moving part of the testing machine. The nodes belonging to the elements modeling the clamped portion of the sample were selected as independent nodes and the dependent node was automatically calculated and renamed node #2.
To simulate the tensile test, a displacement of 300 mm was applied at node #2 (corresponding to the center of the pink RBE3 element in Fig. 3.13). This displacement value was selected to approximate the mean experimentally measured elongation at failure. since the primary objective of this study did not encompass the modeling of sample failure.

Constraints

The original boundary condition was implemented by fully constraining the nodes of the elements belonging to the two sample faces, in directions 1, 2, and 3 (translations along x,y and z axes). However, it was subsequently determined to be more accurate to employ a configuration analogous to the procedure adopted for the Imposed displacement, i.e. using an RBE3 element (blue in Fig. 3.13) and applying the BCs to its central node, node #1. This formulation permits better lateral contraction of the elements, leading to a more visually realistic results.

An additional constraint was imposed on node #2, constraining the translational degree of freedom along the x-axis, in accordance with the standard procedure adopted when a prescribed displacement is specified via a `LOAD` bulk data entry [58].
This two constrains are represented by the dark blue triangles in Fig. 3.11.

Finally, the `Load Step` was created specifying the Imposed displacement as `LOAD` and the Constraints as the `SPC` control card.

It is important to emphasize that the approach adopted in this framework represents a significant simplification of the actual physical behavior. The frictional interaction at the interface between the fixture and the silicone specimen was not negligible, even during the experimental tests. As previously noted, slip phenomena occurred and it was necessary to implement additional measures to prevent the specimens from sliding out of the grips. This modeling choice has certainly influenced the results, and, in order to develop a numerical model that is more representative of the real system than the one presented here, it will be essential to incorporate an appropriate friction coefficient and perhaps even model the grips themselves.

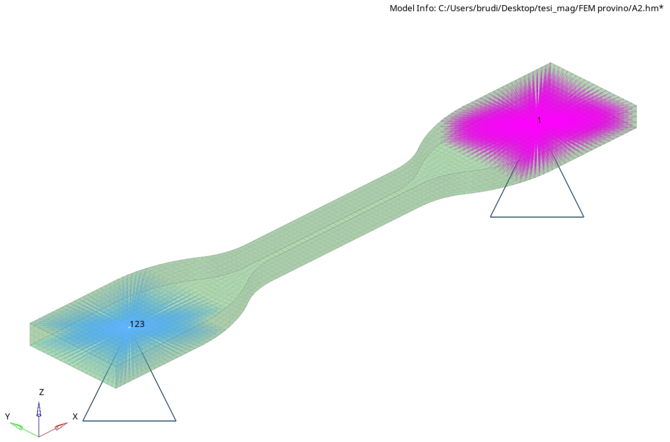

Figure 3.11: a

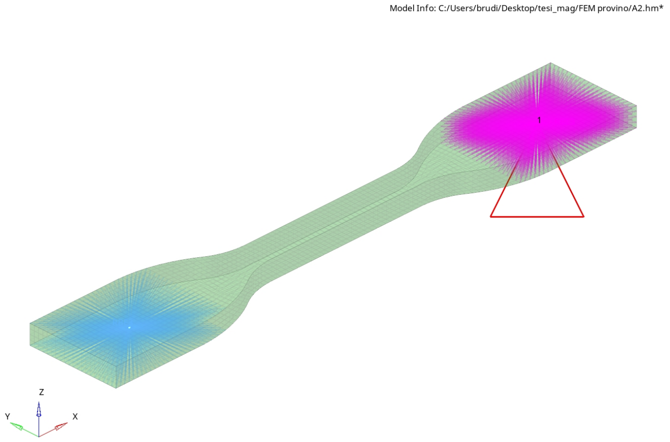

Figure 3.12: b

Figure 3.13: Rigid elements in blue and pink. (a) Constrains definition in dark blue and (b) Imposed displacement in red.

3.4.3 Material Definition

After creating the solid mesh and setting the Boundary Conditions, the material details has to be specified.
To represent the Yeoh hyperelastic model, using the material parameters obtained according to Sec. 3.3, two different approaches were tested, and the one that proved most efficient in terms of convergence was ultimately chosen.

As an initial approach, once the material parameters had been identified via an optimization algorithm implemented in Matlab, ECOFLEX was modeled using the `MATHE` material card in relation to the `PSOLID` property. Within this framework, `YEOH` was selected as the hyperelastic constitutive model, and the corresponding material constants $C10$, $C20$, and $C30$ were assigned the values reported in Tab. 3.3.

A second methodology consisted in directly importing the ECOFLEX tension data response into the software via the `TABLES1` table where the x-values entry are the stretch rations and y-values are the engineering stress [59]. The `MATHE` material card is here employed again, specifying the desired constitutive model, allowing in this case the solver to estimate the material parameters autonomously.
The resulting parameters were subsequently found to be in good agreement with those obtained using the Matlab identification algorithm. Therefore, in this application, the two methodologies can be regarded as essentially equivalent.
The input dataset is reported in the code listing in Appendix listing 6.1.

3.4.4 Load Step Inputs and `PARAM` setting

As discussed in detail in the previous chapters, a hyperelastic material exhibits a non-linear elastic stress–strain response that deviates significantly from the linear behavior predicted by Hooke's law. Furthermore, for this type of test, geometric nonlinearity due to large deformations introduces an additional level of complexity into the analysis.
Therefore, for a nonlinear quasi-static finite element analysis (FEA) of this type, several additional parameters must be specified with particular care in order to obtain a reliable solution.
It is useful at this stage to reiterate the underlying assumptions adopted for this class of materials, namely that they are isotropic and fully, or at least nearly fully, incompressible.

In the following list, the additional parameters are reported as text lines extracted from the solver deck `.fem` file for the sake of conciseness.

- As the max strain is expected to exceed the limit of small deformation theory ($> 5\% - 10\%$), large displacement analysis is activated for all subcases. This was done using the `PARAM` bulk data entry and assigning a value of 1 to `LGDISP`.

```
PARAM, LGDISP , 1
```

- The bulk data entry `NLPARM` was used to divide the load into smaller sub-increments, in order to help the convergence. This number, represented by the field `NINC` was setted on 50.

```
NLPARM          3       100
```

- It is useful to divide the total imposed displacement into smaller incremental steps in order to evaluate convergence at each stage. In this simulation, the overall displacement was partitioned into 20 intervals to output intermediate results. This was done using the `NLOUT` bulk data entry and assigning a value of 20 to the parameter `NINT`.

```
NLOUT          2  NINT          20
```

3.4.5 Results

The true stress–strain response are extracted from the FEA using the *Altair HyperGraph* software and, for the stress-strain curves are evaluated with respect to a central element of the specimen model, so as to minimize the influence of boundary conditions on the computed results.
The results in terms of tensile force and displacement, are evaluated at node #2, which is the dependent node in RBE3 element used for the imposed displacment.

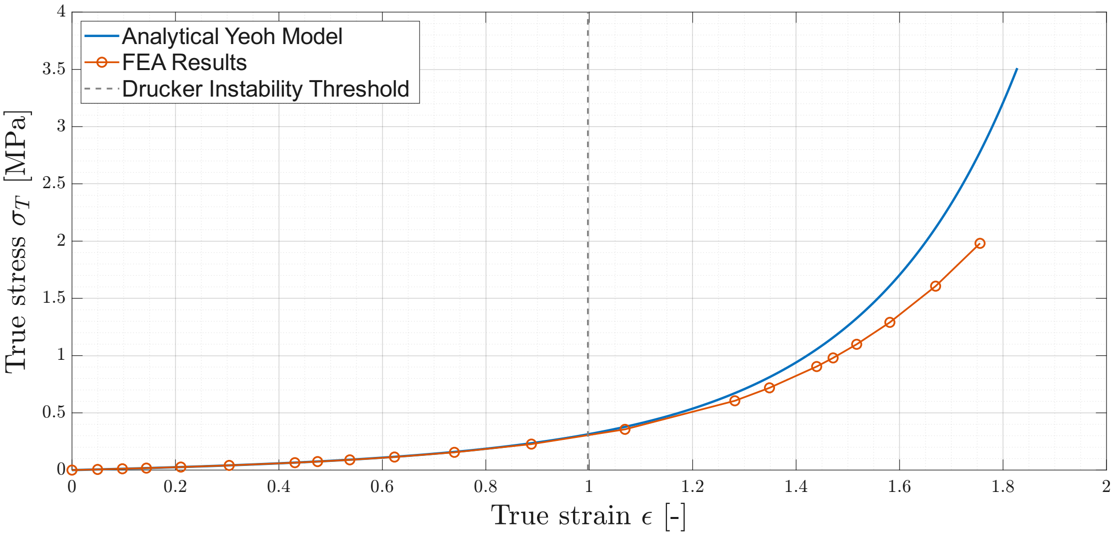

Figure 3.14: FEA results compared to the Yeoh Curve fitted on the experimental dataset and Drucker Instability Threshold

The analysis of the FEA results shows perfect agreement with the Yeoh analytical model up to a unit true strain. Beyond this threshold, a deviation is observed due to numerical instability of the material.

This behavior find a correspondence through the Drucker Stability Check in the OptiStruct output file, performed internally by the solver.

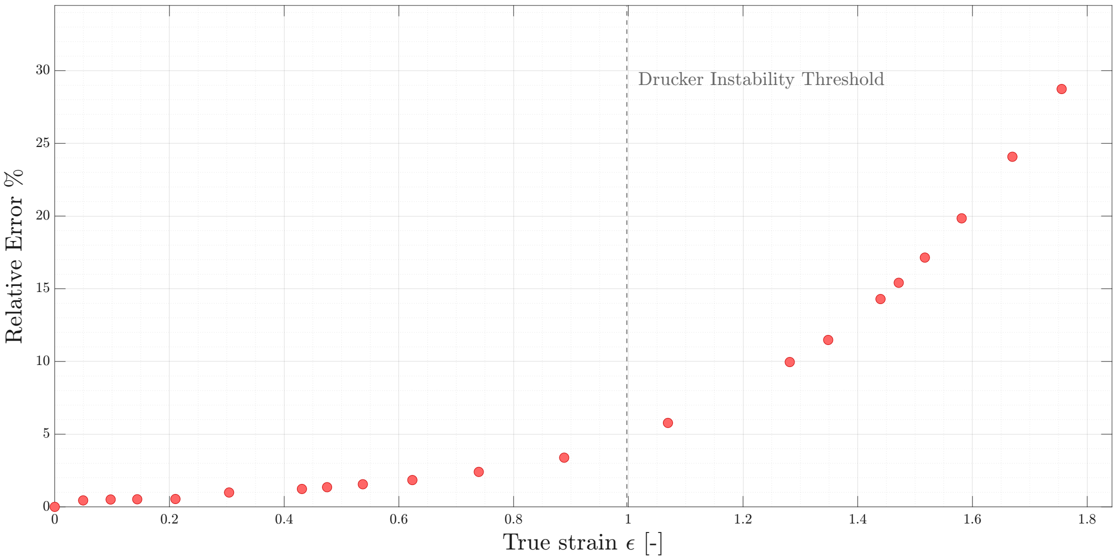

Figure 3.15: Variation of the relative error of the FEA results in terms of true stress as a function of increasing strain. A pronounced escalation of the error becomes apparent once the Drucker instability limit is exceeded.

Drucker's first stability criterion stipulates that an increase in the external influence on the body (such as time, temperature, or load) must result in a positive change in the internal energy. Therefore, energy cannot be released, so the following criterion for the inner product of the tensors has to be fulfilled:

$$\Delta(JT) : \Delta(E_{log}) \geq 0 \tag{3.23}$$

where $J = det[F]$, F is the deformation gradient, T is the Cauchy stress tensor, while E_{log} is the logarithmic strain tensor.
The instability is intrinsic to the resulting hyperelastic coefficients and, although the coefficients C_i are all positive (a necessary condition for global stability), the extremely small value of C_{30} (10^{-14}) makes the contribution of the cubic term negligible within the analyzed strain range (See Eq. 3.19), causing instability.

From the simulation results, it is shown that the model loses stability under biaxial compression (i.e. a stress state corresponding to lateral contraction in uniaxial tension) for nominal strains exceeding 0.9974. However, the material model is declared to be verified to remain stable for all nominal strain levels associated with the other types of loading.

Observing Fig. 3.16 and Fig. 3.14, it is clear that the FEM model is able to follow the trend of the theoretical curves satisfactorily up to the threshold value, after which it diverges and shows a systematic underestimation of stiffness.

For this reason, the material model is considered valid and accurate for values of true strain under the Drucker Instability Threshold of $\epsilon = 0.9974$, while for higher values of strain, the emergence of a local stability limit explains the reduction in stiffness observed in the numerical model relative to the theoretical response, thereby resulting in numerical softening as shown also by the relative error trend shown in Fig. 3.15.

The comparison in terms of the force–displacement response, reported in Fig. 3.16, confirms the reliability of the numerical model up to the onset of the instability threshold, which occurs at a displacement of approximately 110 mm. In this range, the numerical simulation accurately reproduces the trend of the theoretical model, displaying a slightly higher stiffness than the real case, with an error of about 11% that remains essentially constant as the displacement increases (see Fig. 3.17). Beyond the instability point, the FEA curve is no longer able to follow the increase in stiffness predicted by the analytical model, and the relative error shows first a rapid decrease and then a rapid increase.
This behavior is consistent with the numerical softening also observed in the stress–strain diagram, confirming that Drucker's instability limits the solver's capability to represent the material response at large deformations.

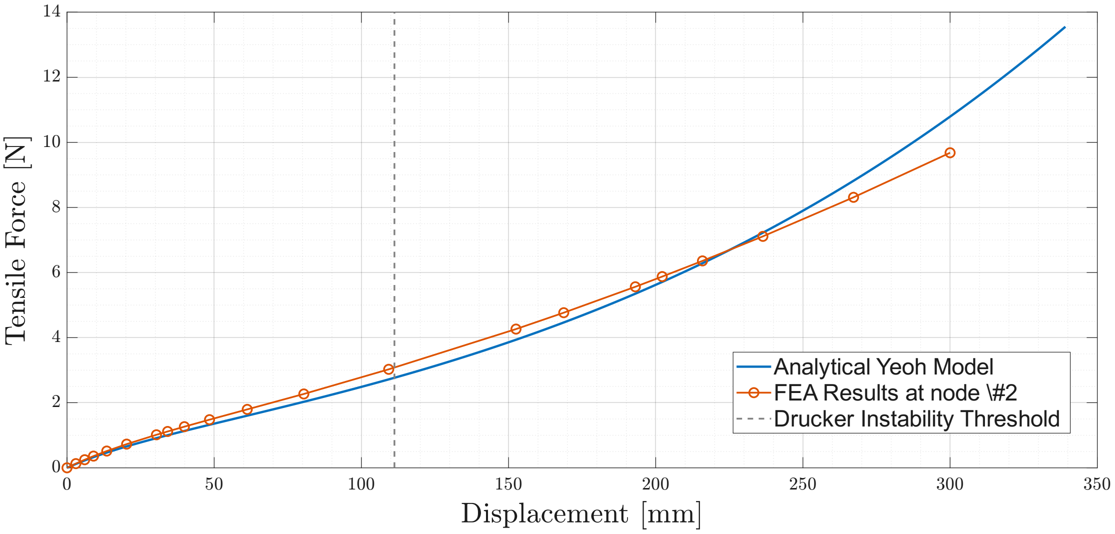

Figure 3.16: FEA results in terms of tensile force, compared to the Yeoh Curve fitted on the experimental dataset and Drucker Instability Threshold.

The distribution of element stress along the geometry and the deformed configuration at displacement of 300 mm is reported in Fig. 3.18. This image shows that the FE simulation has leading to a behavior coherent with the one observed in the experimental tests.

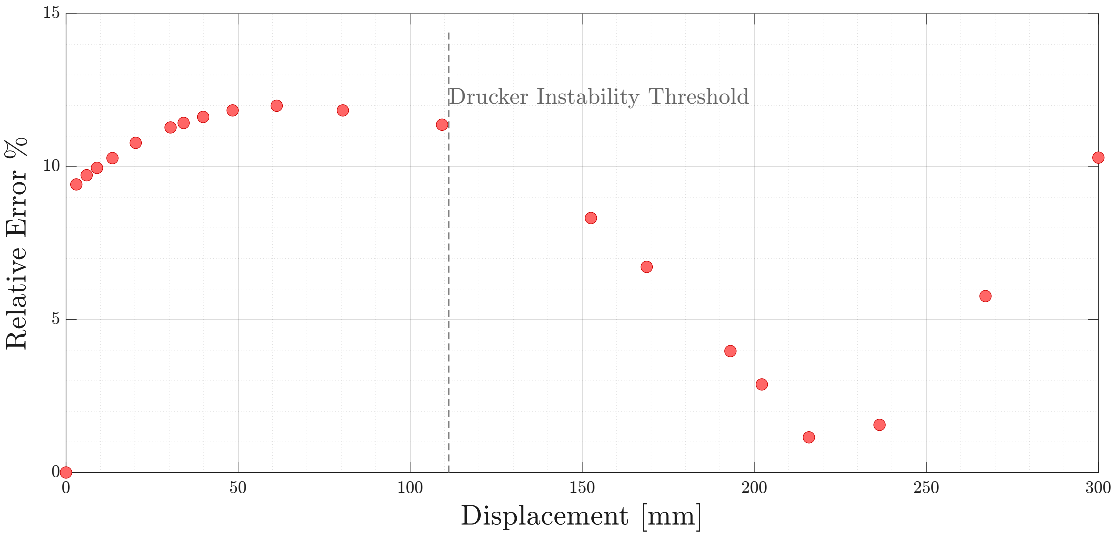

Figure 3.17: Variation of the relative error of the FEA results in terms of tensile force as a function of increasing displacement.

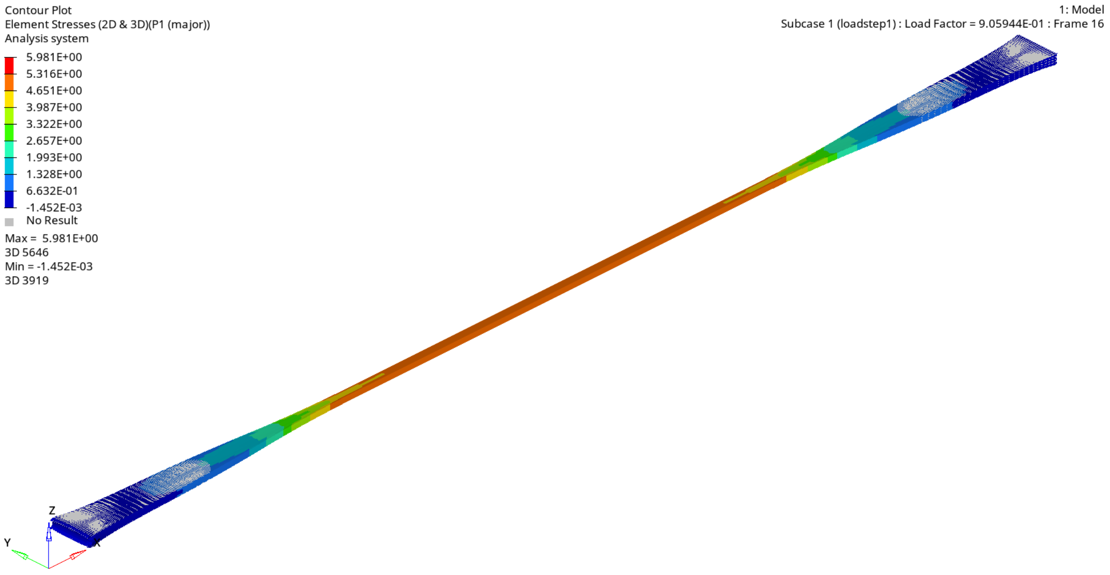

Figure 3.18: Element stress distribution along x direction (major).

Chapter 4

Final Configuration: A Modular Approach

Once the unit cell geometry was selected and the material properties were defined, taking into account both the mechanical requirements and the constraints imposed by the manufacturing process, the modeling effort was extended to the full multi-module actuator assembly.

A key consideration at this stage is that the self-weight of the actuator becomes progressively more significant as the number of stacked modules increases. In a vertically oriented configuration, the gravitational load acts in opposition to the axial elongation driven by internal pressure, effectively reducing the net displacement of the free end. Conversely, during vacuum-driven retraction, the weight of the lower modules assists compression. This asymmetry between the extension and retraction dynamics becomes increasingly pronounced with the number of modules and must be accounted for when interpreting both simulation and experimental results.

To characterize this effect and evaluate the scalability of the design, three assembly configurations were produced and analysed: a 2-cell, a 4-cell, and an 8-cell stack. These configurations allow a direct comparison of elongation and compression behaviour as a function of assembly length, and provide an initial basis for assessing the trade-off between stroke amplitude and structural self-weight.

In addition to elongation analyses, compression analyses were also performed to validate the contact modeling approach; however, simulating hyperelastic materials with interacting surfaces represents one of the most significant challenges in FEM analysis due to the multiple layers of non-linearity involved. While these simulations yielded consistent qualitative results up to a specific contraction percentage, the complexity of the contact mechanics eventually prevented full numerical convergence, leading to their omission from this report. Consequently, an experimental approach was prioritized to accurately characterize the compression dynamics, the details of which are provided in the further below.

4.1 FEA analysis

In parallel with the physical fabrication process, which required a substantial portion of the time devoted to this work due to the various manufacturing challenges that emerged iteratively during the design phase, a finite element analysis was carried out in order to obtain preliminary numerical results on the actuator's mechanical response without waiting for a fully validated physical prototype.

The simulation was performed on a 4-cell modular actuator. The modeling procedure follows the same framework established in Chapter 3 for the characterization of the EcoFlex 00-30 material, in terms of constitutive model selection, element type, and main solver settings. The material was indeed modeled using a Yeoh hyperelastic formulation fitted to the experimental tensile test dataset.

Contact and Symmetry Modelling

The simulation complexity is significantly higher than that of the single-cell analyses, due to the introduction of contact nonlinearity in addition to the geometric and material nonlinearities already present. Contact was modeled for both the outer and inner surfaces of the actuator as self-contact, using PCONT card images. The contact parameters were specified as follows: S2S in the DISCRET field, CONSLI in TRACK, and NORM in MORIENT.

The NLparm and NLout control cards were activated, consistent with the settings used for the tensile specimen simulation, reported in Sec.3.4.4

	CTID	PID	SSID	MSID	MORIENT	[SRCHDIS]	ADJUST
CONTACT	1	9	5	ERROR	NORM	0.900	
	DISCRET	TRACK	CORNER		SORIENT		
	S2S	CONSLI					

Figure 4.1: Contact control card details

Simulating the full geometry of the 4-cell assembly at the required mesh density would have resulted in prohibitively long computation times. To obtain equally valid results at a reduced computational cost, advantage was taken of the axial symmetry of the geometry: only a circumferential sector (one fifth of the full model) was simulated, with appropriate symmetry boundary conditions applied on the

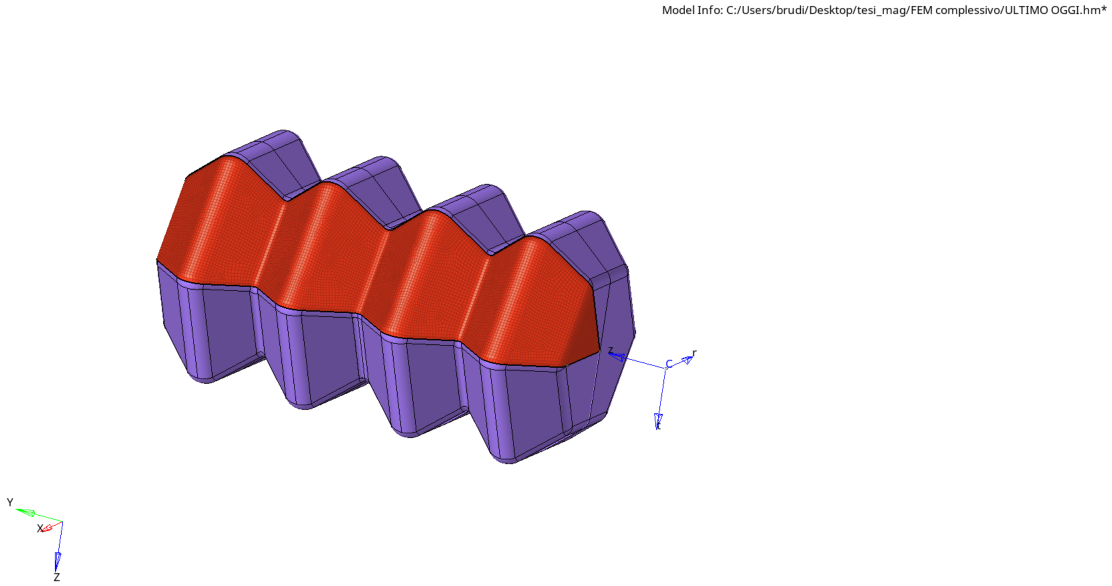

Figure 4.2: 1/5 mesh of the geometry, modeled using symmetry, and both the main reference system and the cylindrical one (in blue)

cut faces. This was implemented by assigning a cylindrical reference frame to the elements belonging to the cut surfaces and constraining degree of freedom 2 (tangential translation) on those elements. Additionally, nodes lying on the central axis of the part were constrained in the radial direction, preventing non-physical rigid body motion. The resulting mesh, with an element size of 0.4 mm and two element layers through the wall thickness, is shown in Fig.4.2.

Boundary Conditions and Loading

The nodes belonging to the top face of the assembly were constrained in all three translational degrees of freedom, representing the fixed attachment point of the actuator. Two separate load collectors were defined to handle positive and negative internal pressure, respectively. Pressure was applied using PLOAD4 cards with a magnitude of 0.003 MPa, (3kPa), distributed over all internal surfaces of the chamber. The pressure magnitude was intentionally selected to be relatively low, as the principal objective of the simulation was to examine the deformation profile and resulting geometry of the actuator rather than to replicate its full operational loading conditions.

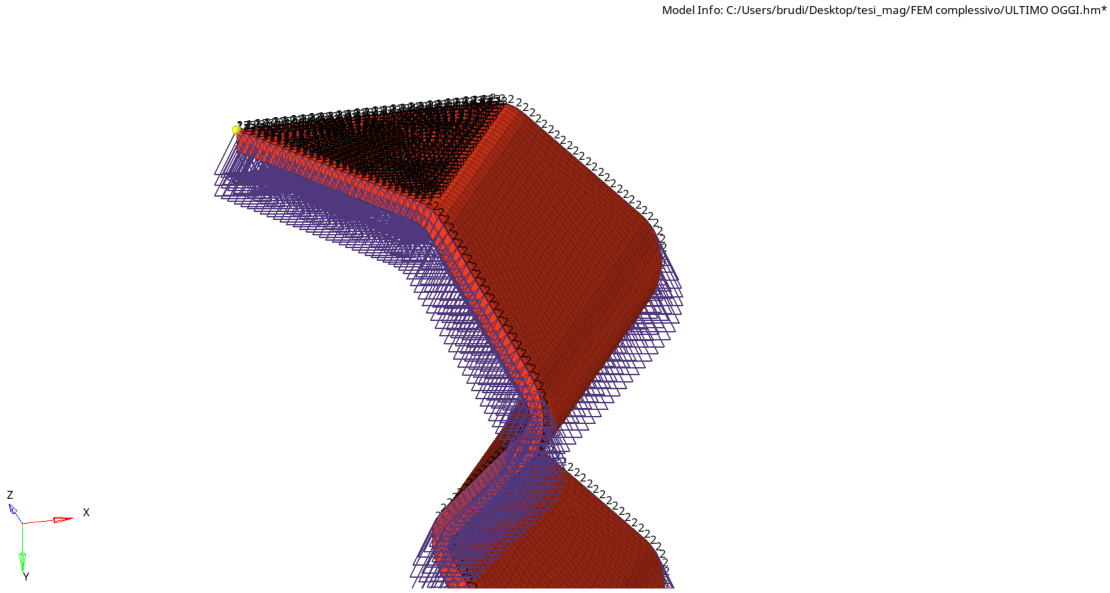

Figure 4.3: Representation of the constraints applied to the structure. The upper surface is constrained in degrees of freedom (DOF) 1, 2, and 3 with respect to the global reference system. Nodes located on the cutting surfaces are constrained in DOF 2 (tangential translation) of the cylindrical reference system, whereas the three nodes lying on the axis are constrained in both DOF 1 and DOF 2.

4.1.1 Results

The key results of the FEA are summarised in Tab.4.1. At a pressure of 6060 60 kPa, the 4-cell assembly reaches a maximum axial displacement of 20.49mm, corresponding to an elongation of 25.46% relative to the rest length. The maximum principal strain is 0.761 and the peak von Mises stress is 0.1399 MPa, both occurring at the most deformed regions of the cell walls, as visible in Fig.4.4.

4.2 Manufacturing

4.2.1 Mould Design and Fabrication Strategy

As discussed in the previous chapter, the final material selection favoured a silicone-based solution, motivated both by the availability of a substantial body of literature on soft pneumatic linear actuators and by the high geometric freedom that casting processes offer compared to alternative fabrication routes. The principal constraint of moulding is that the selected geometry must be physically realisable: the mould must allow complete filling of all internal cavities, and the cured part must be extractable without damage. As will be shown in the following sections, both

Parameter	**Value**	**Unit**
Internal pressure	3	kPa
Material model	Yeoh (fitted dataset)	—
Number of elements (1/5 sector model)	17 640	—
Max displacement	20.49	mm
Elongation	25.46	%
Max principal strain	0.761	—
Max von Mises stress	0.1399	MPa

Table 4.1: Summary of FEA results for the 4-cell assembly at peak pressure.

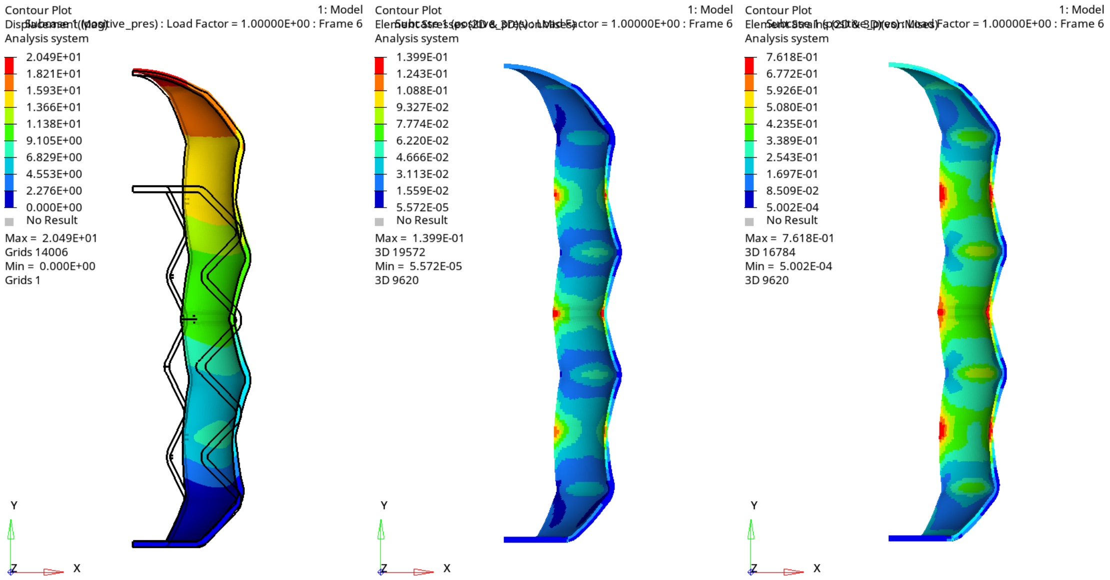

Figure 4.4: Displacement field of the 4-cell assembly under 60 kPa internal pressure (FEA, 1/5 sector model). The color map shows total translation magnitude.

requirements can be satisfied even for geometrically complex configurations through a limited number of deliberate design expedients. It is worth noting, as an aside, that soft lithography represents an alternative fabrication route that is in principle even better suited to complex internal geometries, particularly at small scales. However, it requires a more carefully controlled fabrication environment and more specialised equipment, and was therefore not pursued within the scope of the present work. The mould development followed an iterative process, well represented in

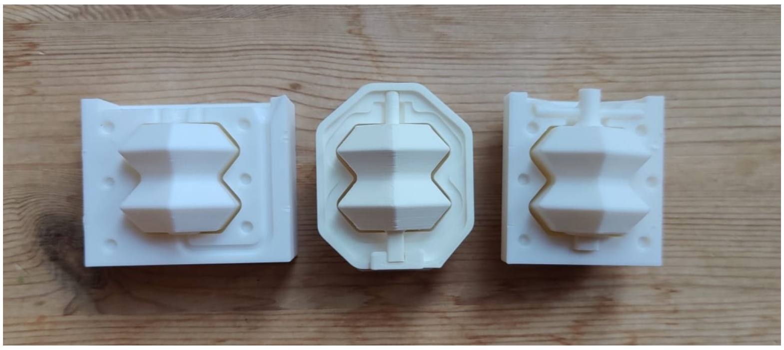

Figure 4.5: Three intermediate mould configurations from the iterative development process. The leftmost version uses a bottom-fed sprue channel designed for injection casting. The intermediate designs, all based on a two-halves concept, achieved high casting quality but could not be reliably joined without interfacial gaps.

Fig.4.5, that went through several intermediate configurations before converging on the final solution. Early designs attempted to fabricate the actuator body in two separate halves, subsequently joined along a longitudinal interface. While this approach achieved high casting quality in the individual halves, no joining strategy could be identified that simultaneously guaranteed precise geometric alignment and complete absence of interfacial gaps — a critical requirement for a pressure-retaining chamber. This class of solutions was therefore abandoned.

The final mould concept instead produces the actuator in three sequential stages:

- Fabrication of the top and bottom end faces, with integrated stiffening discs and pneumatic interface fittings;
- Fabrication of the central body;
- Bonding of the end faces to the central body.

Each of these stages is described in detail in the following subsections.

4.2.2 End Face Fabrication

Two distinct end face geometries are required: a *closed base*, which seals the bottom of the actuator chamber, and an *open base*, which serves to incorporate the pneumatic inlet tube. The mould for the closed base is shown in Fig.4.6; the corresponding open-base mould is shown in Fig.4.7.

For the closed base, the fabrication proceeds in two pours. In the first step, the joining ring is seated in its dedicated housing in the mould base. A first silicone pour is then made. While the silicone is still in the liquid state, the stiffening

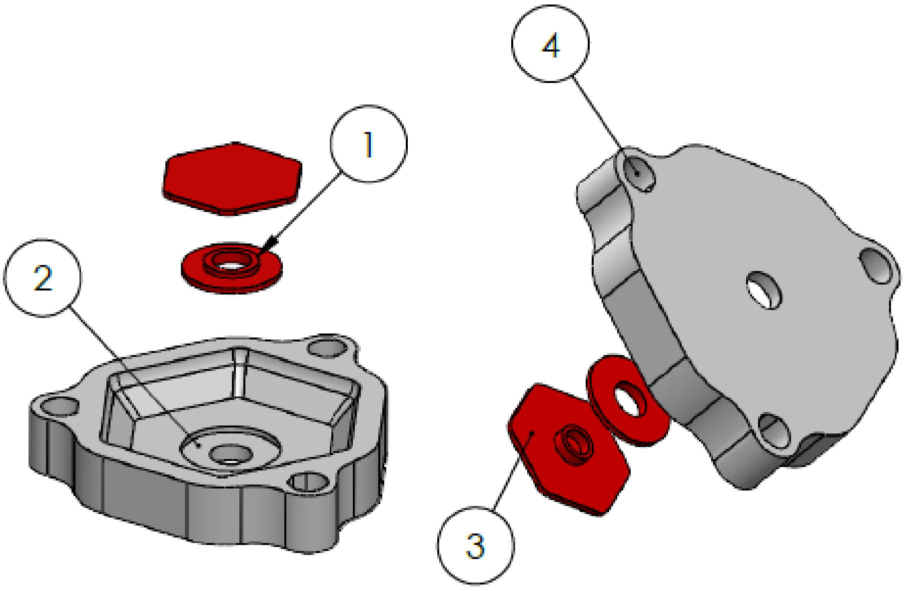

Figure 4.6: Closed-base mould (bottom face, no pneumatic connection). (1) Joining ring with integral spacer shoulder that positions the stiffening disc at the correct depth within the silicone matrix; (2) housing for the joining ring; (3) stiffening disc; (4) alignment bolt holes.

disc is placed onto the free surface, carefully aligned with the ring below. The disc is not bonded to the silicone by adhesive — as will be discussed in Section 4.2.4, no adhesive has been found to bond reliably to cured EcoFlex — but is instead embedded within the silicone matrix during the subsequent bonding step, where a second pour simultaneously encapsulates the disc and joins the face to the body. This approach exploits friction and geometric interlocking within the silicone matrix to achieve structural continuity between the rigid insert and the elastomeric substrate.

The open base is fabricated by an essentially identical procedure, with one additional element: the pneumatic inlet tube must be correctly positioned so that its upper surface is flush with the top surface of the stiffening ring. This alignment is critical because the tube will later be sealed to the joining ring from the outside using adhesive, after the base has been bonded to the body. Correct flush positioning ensures that the sealed interface is accessible and that no silicone occludes the tube bore during the pour.

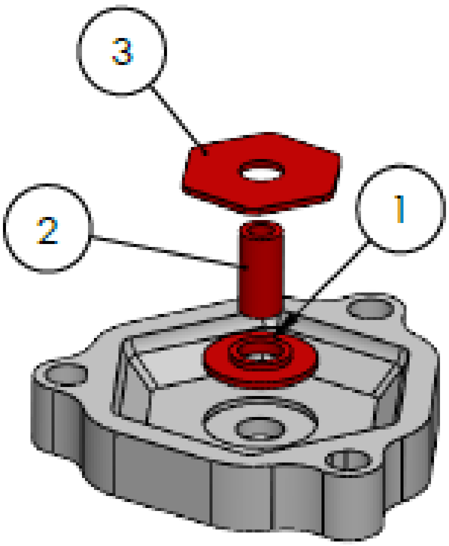

Figure 4.7: Open-base mould (top face, pneumatic inlet). (1) Joining ring with housing; (2) pneumatic inlet tube, positioned flush with the ring top surface; (3) stiffening ring with central bore, bonded to the tube during encapsulation.

4.2.3 Central Body Fabrication

The central body mould assembly sequence is illustrated in Figs. 4.8 and 4.9. The mould consists of four main components: a base piece that houses the inner core (mandrel), two lateral half-shells that define the outer geometry of the body, and a top closing piece that forms the interface surface for bonding with the end faces. The lateral shells are split into two symmetric halves to allow correct positioning around the core without interference, and are aligned and locked by lateral pins inserted through the corresponding holes. Alignment between all components is ensured by dedicated guide pins and mating features.

Silicone is poured from the open perimeter at the top of the assembled mould, introduced gradually using a syringe to minimise air entrapment, and the level is monitored over the first few minutes to top up any volume lost to settling or minor leakage. Demoulding is facilitated by dedicated extraction holes in the base and push-out points distributed over the body surfaces, as labelled in Fig. 4.9.

For configurations that incorporate internal stiffening rings — intended to limit radial expansion, as discussed in Section 4.2.5 — the pour must be interrupted at each ring insertion level. The procedure is as follows: silicone is poured up to

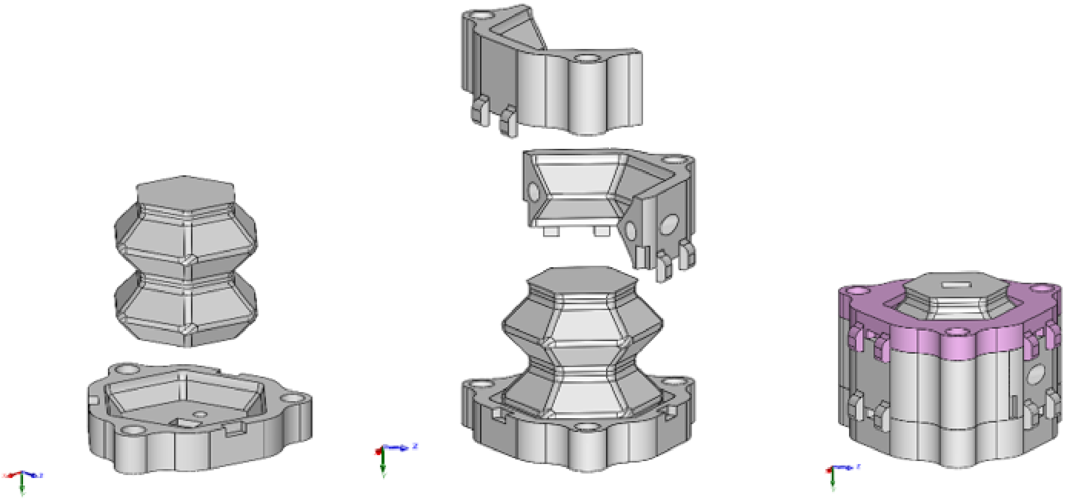

Figure 4.8: Body mould assembly sequence. Left: the mandrel (core) is inserted into the base housing. Centre: the two lateral half-shells are positioned around the core. Right: the top closing piece (shown in pink) is placed to define the bonding interface surface on the finished part.

the elevation corresponding to the first ring location; the ring is then placed on the free surface in the correct radial position; the pour is paused until the silicone has gelled sufficiently to hold the ring in place; the next mould stage is assembled; and pouring resumes. This sequence is repeated once for each ring, meaning the total number of pour interruptions equals the number of rings plus one. The main challenge in this procedure is the precise centring of each ring within the wall cross-section: the ring must sit at mid-thickness so that it is fully encapsulated on both sides, ensuring that the internal surface of the chamber remains sealed. Any misalignment that allows the ring to contact the core creates a gap through which pressurised air can bypass the silicone wall, rapidly leading to chamber failure and ring displacement. This issue is discussed further in Section 4.2.4.

An important feature of the body mould design is the interlocking socket visible in Fig. 4.9, which allows multiple central body modules to be stacked and aligned precisely before bonding. This feature is what makes the modular architecture truly scalable: the body fabrication sequence can in principle be repeated an arbitrary number of times, and any number of modules can be stacked to produce actuators of any desired length, without redesigning or remaking any component of the mould.

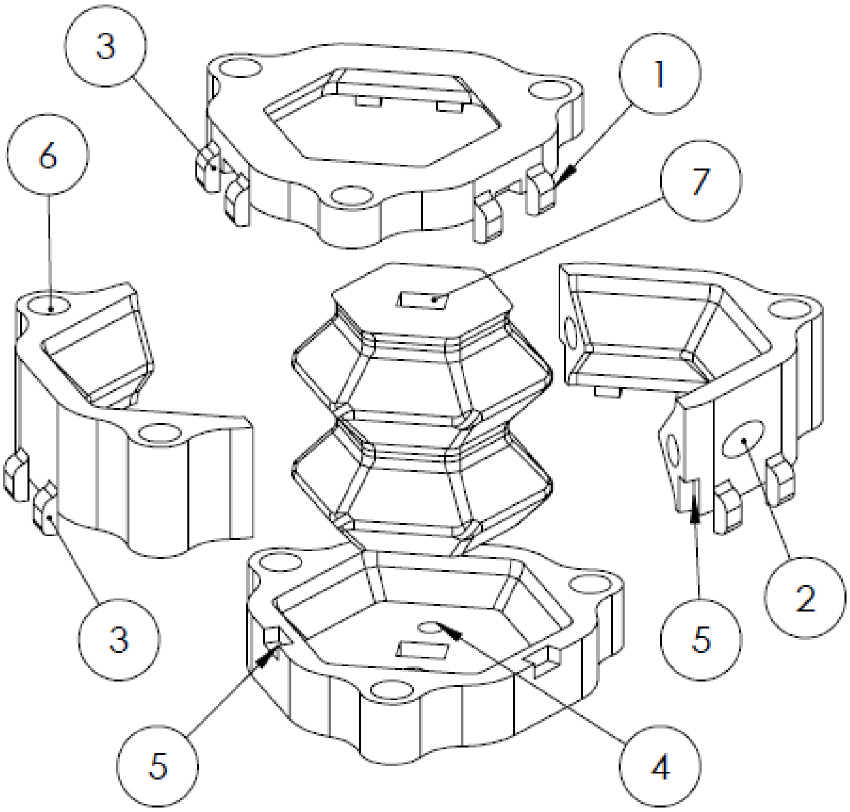

Figure 4.9: Exploded view of the body mould. (1,3) Alignment feet ensuring correct lateral panel registration; (2) lateral pin holes for panel stiffening; (4) core extraction holes; (5) demoulding push-out points; (6) bolt alignment holes; (7) modular core socket for multi-module assemblies.

4.2.4 Bonding Strategy

The bonding of the end faces to the central body deserves particular attention, as it represents one of the most delicate steps of the entire fabrication process and the one that required the most iterative development. The fundamental difficulty is that cured silicone elastomers — and EcoFlex in particular — exhibit extremely low surface energy, which prevents virtually all commercial adhesives from forming a reliable bond. Testing confirmed that applying uncured silicone as an adhesive between two already-cured surfaces produces no structural joint: the thin layer does not cure correctly in the confined interface and, even when it does, the resulting bond fails at negligible loads. This behaviour is well documented in the soft robotics fabrication literature and is the reason why most multi-part silicone assemblies rely instead on co-curing — casting one part directly against another that is either uncured or only partially cured, so that the polymer networks form across the interface and create a chemically continuous joint. The bonding strategy adopted here exploits precisely this principle. When the end face is bonded to the body, the mould is reassembled in its full configuration, and a fresh silicone pour is made into the gap between the face and the body. This gap is deliberately sized to accommodate a minimum silicone layer thickness sufficient for complete crosslinking — empirically determined to be approximately 1.5 mm for EcoFlex 00-30 under the mixing and curing conditions used. The mould therefore serves a dual function: it is both the forming tool for the individual parts and the fixture that holds them at the correct spacing during the bonding pour, eliminating the need for any additional jigs or clamps.

The same principle was applied, with favourable results, to the bonding of the pneumatic interface fittings. The inlet tube and its associated ring were designed so that they could be embedded in a silicone pour during the face fabrication step, achieving a robust mechanical connection through encapsulation rather than adhesive bonding. This solution proved reliable across all samples tested and is considered one of the more successful outcomes of the iterative design process.

4.2.5 Open Challenges and Directions for Future Development

FEA and experiments show that, in its current form, the actuator wastes much of the input pressure in radial expansion instead of axial elongation. As discussed in Sec.2.1, this is an inherent limitation of isotropic silicone actuators and was only partially mitigated by geometry optimization. Analytical and numerical results indicate that geometry alone cannot eliminate radial bulging at higher pressures; a structural radial constraint is required to achieve the efficiency of an origami-type geometry.

This issue has been widely studied for fiber-reinforced and mesh-constrained actuators. Martinez et al.[60] showed that inextensible fibers embedded in an elastomer can suppress deformation along chosen directions, programming the actuator's shape change. Li et al.[61] used an inextensible mesh sleeve around the silicone body to limit radial expansion while leaving axial motion free. Both approaches introduce anisotropic stiffness elements that are axially compliant but radially stiff.

For the present geometry, two main strategies are promising. The first is an external constraint: a sleeve or lattice wrapped around the actuator to cap radial

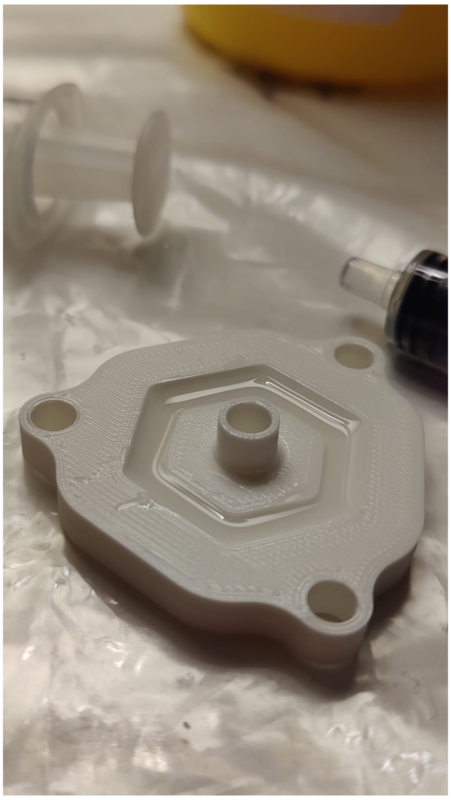

Figure 4.10: Open-base fabrication: the pneumatic inlet tube is visible, positioned concentrically with the stiffening ring. In the subsequent bonding step, the upper face will be joined to the body and the stiffening disc will be fully encapsulated within the silicone matrix.

displacement. An origami-inspired sleeve, such as Kresling or Miura-ori, is attractive because it is naturally axially compliant and radially stiff, complementing the silicone core. A rigid-jointed lattice with tuned hinge compliance is a simpler, easily 3D-printable alternative.

The second is the embedded ring strategy used here: rigid annular inserts placed in the silicone wall at locations of peak radial displacement. As noted in Section4.2.4, this approach faced practical issues with insert positioning and chamber sealing, and a robust implementation was not achieved. However, the concept is sound and the failure mechanisms are understood. With a mould tailored for ring insertion — for example, with radial guides holding the ring at mid-thickness during pouring — and a ring design that maintains a minimum silicone layer between the ring's inner face and the core, this strategy should be feasible. It remains an open and high-priority direction for future work.

Figure 4.11: Working table during the fabrication campaign, showing samples at various stages of the production process and the auxiliary tools used.

4.3 Preliminary Testing

Once physical samples were available, a qualitative testing campaign was carried out to assess the actuator's behavior under real operating conditions and to verify the deformation modes predicted by the FEA. The samples were connected to a pneumatic circuit that allowed both positive pressure and vacuum to be applied and released, enabling observation of both the extension and retraction phases of the actuation cycle.

4.3.1 Test Setup

The pneumatic circuit, shown schematically in Fig.4.12, consists of a compressor and a vacuum pump, each connected to its own manual isolation valve that allows independent control of the pressure supply and the vacuum line. Both feeds are connected in parallel to the actuator inlet, with a differential pressure gauge inserted in parallel to monitor the internal pressure relative to ambient. The gauge was selected for its sensitivity in the low-pressure range relevant to this application.

It should be noted that all valves used in this preliminary setup were analogue (manually operated), which precluded precise or repeatable pressure control and introduced non-negligible dead volumes in the tubing that were not systematically accounted for in the pressure readings. As a consequence, the pressure values reported in Tab.4.2 should be considered indicative rather than precisely calibrated. A digitally controlled valve system with electronic pressure regulation would be required for a quantitative characterization, and is identified as a priority for future experimental development.

To monitor axial displacement during actuation, a millimeter-ruled sheet (each square corresponds to 5x5 mm) was placed behind the actuator as a reference scale, and the tests were recorded on video. Displacement was then estimated by correlating the video frames with the scale reference. However, the frame rate of the camera used was insufficient to resolve the rapid deformation events with the temporal resolution needed for a quantitative dynamic analysis. As a result, the displacement data extracted from this campaign are again to be regarded as qualitative indicators of the actuator's behavior rather than precise measurements.

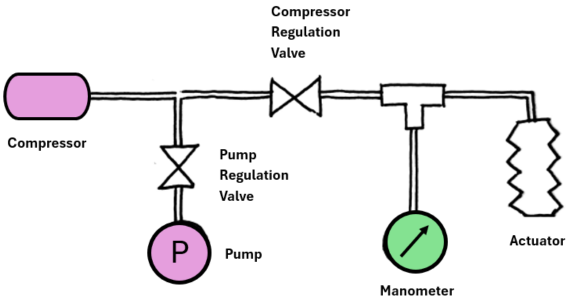

Figure 4.12: Simplified schematic of the pneumatic test setup. Compressor and vacuum pump with isolation valves, differential pressure gauge, and actuator inlet are shown.

4.3.2 Results and Observations

The performance data collected across the three actuator configurations are summarized in Tab. 4.2. The expansion ratio, defined as the ratio of maximum extended length to minimum compressed length L_{max}/L_{min}, is the primary figure of merit adopted for this comparison, as it captures the overall stroke efficiency of each configuration independently of its absolute size.

The 2-cell and 4-cell configurations both demonstrated the expected accordion-like compression and extension behavior. The expansion ratio increases from 4.684.68 4.68 to 5.385.38 5.38 between the 2-cell and 4-cell assemblies, suggesting a modest but consistent improvement in stroke efficiency as the number of modules grows. This trend is physically plausible: in a longer stack, the end effects — where the terminal cells are constrained by the attachment interfaces — represent a smaller

Figure 4.13: Frames from the dynamic behavior of the 2 units actuator during compression.

Figure 4.14: Frames from the dynamic behavior of the 4 units actuator during compression.

fraction of the total assembly, and the interior cells deform more freely, contributing more efficiently to the net stroke.

The 8-cell configuration, however, did not achieve full accordion compression under the vacuum levels tested, as it is visible in Fig. 4.15. Instead of folding uniformly along the axial direction, the assembly buckled laterally and collapsed under its own weight along the longitudinal axis, preventing the individual cells from reaching their minimum compressed length. This behavior is a direct consequence of the self-weight: at eight modules, the gravitational load on the lower portion of the stack exceeds the restoring force that the vacuum can generate locally in each cell, causing the assembly to become structurally unstable before full compression is achieved. This represents a practical upper limit on the number of modules that can be effectively tested in a vertically oriented, free-hanging configuration.

Figure 4.15: Initial and final frames from the 8-unit specimen under compression. Note that the deformed geometry of the "compressed" specimen deviates from the predicted shape, most likely due to the influence of self-weight.

Parameter	**2-Cell**	**4-Module**	**8-Module**	**Unit**
Number of modules/cells	2	4	8	-
Max expansion pressure	5.5	32.0	-	kPa
Min full compression pressure	1.7	-	-	kPa
Rest length (L_{rest})	41.0	82.0	164.0	mm
Minimum length (L_{min})	2.2	3.25	-	mm
Maximum length (L_{max})	10.3	17.5	30.0	mm
Expansion ratio	**4.68**	**5.38**	**-**	**-**

Table 4.2: Performance characteristics comparison across 2, 4, and 8-module actuator configurations.

A straightforward approach to decouple the self-weight effect from the actuator's intrinsic mechanical performance would be to carry out compression tests in a neutrally buoyant environment, for instance a near-frictionless horizontal surface such as an oil-lubricated flat plate, so that the actuator's weight is supported externally and does not interfere with the axial force balance. Such tests are identified as a key direction for future experimental work, along with the implementation of a digitally controlled test rig capable of delivering precise, repeatable pressure profiles and synchronized high-speed video acquisition.

Chapter 5

Conclusions

This thesis presented the preliminary design, material characterization, numerical modeling, and initial experimental testing of a soft pneumatic actuator inspired by the ballistic tongue projection mechanism of the chameleon. The work was framed from the outset as a first step toward a more complete biomimetic system, and should be read as such: rather than a fully validated and optimized actuator, what is presented here is a carefully reasoned foundation upon which a functional, biologically faithful device can be progressively constructed. The biological analysis conducted in Chapter 1 revealed the extraordinary mechanical sophistication of the chameleon's hyolingual apparatus, and highlighted an open scientific question — the precise mechanical contribution of the hyoid bone to the efficiency of elastic discharge — that motivated the broader engineering goal of this work. Understanding this contribution in a controlled, experimental setting requires a robotic analogue of sufficient fidelity, and the present prototype represents the first component of that system: a soft pneumatic actuator serving as the tongue retractor and potential protractor element, designed to be subsequently integrated with a structural hyoid scaffold.

The design process of the unit cell, described in Chapter 2, was characterized throughout by a deliberately iterative, trial-and-error methodology. Six candidate unit cell geometries were evaluated analytically and numerically, and the hexagonal trapezoidal geometry (Model 2A) was selected on the basis of its balanced combination of axial volumetric sensitivity, favorable axial-to-radial force ratio, and geometric edge stiffness. The choice of Ecoflex 00-30 silicone as the actuator material and of pneumatic actuation as the power supply strategy were both justified on functional grounds: the former for its compliance, biocompatibility, and elastic energy storage capacity; the latter as the only actuation principle capable of delivering the ballistic acceleration required by the biological reference system.

The material characterization campaign of Chapter 3 produced a calibrated Yeoh hyperelastic model for Ecoflex 00-30, validated against uniaxial tensile test data from nine specimens. The Yeoh model achieved the best fit among the three constitutive models evaluated, with an R^2 of 0.9924. The FEM validation confirmed agreement with the analytical model up to a true strain of approximately 0.997, beyond which Drucker instability caused numerical softening. This limit defines the operational range within which the FEA predictions can be considered reliable, and should be taken into account in future simulations at higher strain levels. The experimental campaign also highlighted a practical manufacturing challenge: air bubble entrapment during casting reduced the percent elongation at break to 480%, well below the 900% reported in the material datasheet, due to void-induced crack initiation. While this did not affect the intrinsic stiffness of the material in the operating range of the prototype, it underscores the importance of improving casting procedures, for instance through vacuum degassing, in future fabrication iterations.

The manufacturing process, documented in Section 4.2, was one of the most demanding aspects of the work, and the iterative development of the mould design consumed a substantial portion of the available project time. The key challenge of bonding cured EcoFlex components was resolved through a co-curing strategy, in which fresh silicone is cast into a deliberate gap between already-cured parts, forming a chemically continuous joint without adhesives. This solution proved reliable and is one of the most transferable outcomes of this work for future fabrication efforts. The embedding of pneumatic fittings by encapsulation during casting was similarly successful. By contrast, the integration of internal stiffening rings, intended to suppress radial expansion, encountered persistent difficulties related to precise ring positioning within the wall cross-section, and a fully satisfactory solution was not achieved within the scope of this work. Although this issue remains unresolved, the failure modes are well understood, and a dedicated mould geometry with radial positioning guides is identified as the most direct path to a viable solution.

The preliminary testing campaign of Section 4.3 confirmed that the 2-cell and 4-cell actuator configurations exhibit the expected accordion-like compression and extension behavior, with expansion ratios of 4.68 and 5.38 respectively, and a trend of improving stroke efficiency with increasing module count. The 8-cell configuration revealed a practical upper limit on free-hanging assembly length, as self-weight induced lateral buckling before full compression could be achieved under the vacuum levels tested. This result, rather than being a failure, provides a concrete and quantified design constraint that must be incorporated into future configurations.

Taken together, the results of this thesis, including both what functioned well and, crucially, what did not, constitute a documented and physically grounded starting point for the continued development of the system. Several directions for future work emerge directly from the findings. In the near term, the most impactful improvements would be the implementation of vacuum degassing during silicone casting to eliminate air bubble defects; the redesign of the stiffening ring insertion procedure to achieve reliable mid-wall positioning and suppress radial expansion; and the replacement of the manual pneumatic test rig with a digitally controlled system with electronic pressure regulation and synchronized high-speed video acquisition, which would enable fully quantitative dynamic characterization of the actuator. At the system level, the integration of an origami-inspired or lattice-type external constraint sleeve — particularly a Kresling-pattern structure, which is naturally radially stiff and axially compliant — represents a promising route to recovering the actuation efficiency that the isotropic silicone material cannot provide on its own. In parallel, the 3D-printed origami variant using flexible elastomeric filaments remains a relevant alternative design direction, particularly if lightweight construction and high stroke-to-rest-length ratio become primary performance objectives once the basic architecture has been validated on the silicone platform.

Looking further ahead, the integration of the soft actuator with a structural hyoid bone analogue, a rigid central scaffold around which the actuator is mounted, remains the primary scientific objective that motivated this work from the outset. This combined system would, for the first time, allow the mechanical contribution of the hyoid geometry to tongue projection efficiency to be isolated and quantitatively characterized in an experimental robotic context, directly addressing the open biological question identified in Chapter 1. The present prototype provides all the necessary foundational elements to make that next step tractable: a characterized material model, a validated FEM framework, a reproducible manufacturing process, and a modular architecture that can be extended in length and adapted in geometry without redesigning its basic components. In this sense, the work presented here is not a conclusion but, deliberately and by design, a beginning.

Chapter 6

Appendix

Listing 6.1: `TABLES1` for ECOFLEX material input in Optistruct `MATHE` material card.

```
Stretch          Stress(test)
1                0
1.1370377118706  0.008896545407685
1.2740754237411  0.016102720930309
1.4111131356117  0.022242016390799
1.5481508474822  0.027674926616353
1.6851885593528  0.032621684707728
1.8222262712234  0.037223026562602
1.9592639830939  0.041572327816306
2.0963016949645  0.045733550990093
2.233339406835   0.049751736941631
2.3703771187056  0.053659381591876
2.5074148305762  0.057480444332298
2.6444525424467  0.061232942812668
2.7814902543173  0.064930676697054
2.9185279661879  0.068584399446537
3.0555656780584  0.072202631483289
3.192603389929   0.075792235099558
3.3296411017995  0.079358827863291
3.4666788136701  0.0829070845366
3.6037165255407  0.086440960748804
3.7407542374112  0.089963860917075
3.8777919492818  0.093478765886411
4.0148296611523  0.096988331092866
4.1518673730229  0.10049496289992
4.2889050848935  0.10400087859479
4.425942796764   0.10750815402714
4.5629805086346  0.11101876181318
4.7000182205051  0.11453460227252
4.8370559323757  0.11805752872088
4.9740936442463  0.12158936834495
```

```
5.1111313561168  0.12513193959387
5.2481690679874  0.1286870668052
5.3852067798579  0.13225659262103
5.5222444917285  0.1358423886273
5.6592822035991  0.13944636455633
5.7963199154696  0.14307047632083
5.9333576273402  0.14671673309301
6.0703953392107  0.15038720359897
6.2074330510813  0.15408402176558
6.3444707629519  0.15780939183043
6.4815084748224  0.16156559300467
6.618546186693   0.16535498376203
6.7555838985636  0.16918000581413
6.8926216104341  0.1730431878213
7.0296593223047  0.17694714887992
7.1666970341752  0.18089460182002
7.3037347460458  0.18488835634143
7.4407724579164  0.18893132201194
7.5778101697869  0.19302651114738
7.7148478816575  0.19717704159011
7.851885593528   0.2013861394001
7.9889233053986  0.2056571414704
8.1259610172692  0.20999349807718
8.2629987291397  0.21439877537288
8.4000364410103  0.21887665782991
8.5370741528808  0.22343095064113
8.6741118647514  0.22806558208255
8.811149576622   0.23278460584297
8.9481872884925  0.23759220332447
9.0852250003631  0.24249268591732
9.2222627122336  0.24749049725233
9.3593004241042  0.25259021543323
9.4963381359748  0.25779655525134
9.6333758478453  0.26311437038462
9.7704135597159  0.26854865558278
9.9074512715865  0.27410454883996
10.044488983457  0.27978733355641
10.181526695328  0.28560244069025
10.318564407198  0.29155545090043
10.455602119069  0.29765209668174
10.592639830939  0.3038982644928
10.72967754281   0.3102999968776
10.86671525468   0.31686349458131
11.003752966551  0.32359511866099
11.140790678421  0.33050139259153
11.277828390292  0.33758900436747
11.414866102163  0.34486480860095
11.551903814033  0.35233582861626
11.688941525904  0.36000925854119
```

```
11.825979237774  0.3678924653956
11.963016949645  0.37599299117741
12.100054661515  0.38431855494615
12.237092373386  0.39287705490452
12.374130085257  0.40167657047785
12.511167797127  0.41072536439187
12.648205508998  0.42003188474883
12.785243220868  0.42960476710209
12.922280932739  0.43945283652945
13.059318644609  0.44958510970506
13.19635635648   0.46001079697041
13.33339406835   0.47073930440402
13.470431780221  0.48178023589036
13.607469492092  0.4931433951878
13.744507203962  0.50483878799572
13.881544915833  0.5168766240209
14.018582627703  0.5292673190432
14.155620339574  0.54202149698061
14.292658051444  0.55514999195372
14.429695763315  0.56866385034956
14.566733475186  0.58257433288505
```

Bibliography

[1] Janine M Benyus et al. *Biomimicry: Innovation inspired by nature*. Vol. 688136915. Morrow New York, 1997 (cit. on p. 2).

[2] Sangbae Kim, Cecilia Laschi, and Barry Trimmer. «Soft robotics: a bioinspired evolution in robotics». In: *Trends in Biotechnology* 31.5 (May 2013). DOI: `10.1016/j.tibtech.2013.03.002` (cit. on pp. 2, 3).

[3] Stephen Coyle, Carmel Majidi, Philip LeDuc, and K. Jimmy Hsia. «Bioinspired soft robotics: Material selection, actuation, and design». In: *Extreme Mechanics Letters* 22 (July 2018). DOI: `10.1016/j.eml.2018.05.003` (cit. on pp. 2, 3, 31).

[4] Yoël Forterre, Jan M Skotheim, Jacques Dumais, and Lakshminarayanan Mahadevan. «How the Venus flytrap snaps». In: *Nature* 433.7024 (2005) (cit. on p. 3).

[5] S. N. Patek, B. N. Nowroozi, J. E. Baio, R. L. Caldwell, and A. P. Summers. «Linkage mechanics and power amplification of the mantis shrimp's strike». In: *Journal of Experimental Biology* 210.20 (Oct. 15, 2007). DOI: `10.1242/jeb.006486` (cit. on pp. 3, 14–16).

[6] Shuzhen Wei and Tushar K. Ghosh. «Bioinspired Structures for Soft Actuators». In: *Advanced Materials Technologies* 7.10 (Oct. 2022). DOI: `10.1002/admt.202101521` (cit. on p. 3).

[7] Weidong Li, Diangang Hu, and Lei Yang. «Actuation Mechanisms and Applications for Soft Robots: A Comprehensive Review». In: *Applied Sciences* 13.16 (Aug. 15, 2023). DOI: `10.3390/app13169255` (cit. on pp. 3, 5).

[8] Cecilia Laschi, Matteo Cianchetti, Barbara Mazzolai, Laura Margheri, Maurizio Follador, and Paolo Dario. «Soft Robot Arm Inspired by the Octopus». In: *Advanced Robotics* 26.7 (Jan. 2012). DOI: `10.1163/156855312X626343` (cit. on p. 4).

[9] Panagiotis Polygerinos, Stacey Lyne, Zheng Wang, Luis Nicolini, Bobak Mosadegh, George Whitesides, and Conor Walsh. *Towards a soft pneumatic glove for hand rehabilitation*. Journal Abbreviation: Proceedings of the ... IEEE/RSJ International Conference on Intelligent Robots and Systems. IEEE/RSJ International Conference on Intelligent Robots and Systems Pages: 1517 Publication Title: Proceedings of the ... IEEE/RSJ International Conference on Intelligent Robots and Systems. IEEE/RSJ International Conference on Intelligent Robots and Systems. Nov. 1, 2013. DOI: `10.1109/IROS.2013.6696549` (cit. on p. 4).

[10] Yichao Tang, Yinding Chi, Jiefeng Sun, Tzu-Hao Huang, Omid H. Maghsoudi, Andrew Spence, Jianguo Zhao, Hao Su, and Jie Yin. «Leveraging elastic instabilities for amplified performance: Spine-inspired high-speed and high-force soft robots». In: *Science Advances* 6.19 (May 8, 2020). DOI: `10.1126/sciadv.aaz6912` (cit. on p. 5).

[11] John D Madden, Nathan Vandesteeg, Patrick A Anquetil, Peter G Madden, Arash Takshi, Serge R Lafontaine, Paul A Wieringa, and Ian W Hunter. «Artificial Muscle Technology: Physical Principles and Naval Prospects». In: () (cit. on p. 4).

[12] Robert Shepherd, Filip Ilievski, Wonjae Choi, Stephen Morin, Adam Stokes, Aaron Mazzeo, Xin Chen, Michael Wang, and George Whitesides. «Multigait Soft Robot». In: *Proceedings of the National Academy of Sciences of the United States of America* 108 (Nov. 28, 2011). DOI: `10.1073/pnas.1116564108` (cit. on pp. 5, 7).

[13] Martin Manns, Jorge Morales Avalos, and Peter Frohn-Sörensen. *Additive manufacturing of silicon based PneuNets as soft robotic actuators*. Vol. 72. Journal Abbreviation: Procedia CIRP Publication Title: Procedia CIRP. June 27, 2018. DOI: `10.1016/j.procir.2018.03.186` (cit. on p. 5).

[14] Michael Wehner, Ryan L Truby, Daniel J Fitzgerald, Bobak Mosadegh, George M Whitesides, Jennifer A Lewis, and Robert J Wood. «An integrated design and fabrication strategy for entirely soft, autonomous robots». In: *nature* 536.7617 (2016) (cit. on p. 5).

[15] Sangok Seok, Cagdas Denizel Onal, Kyu-Jin Cho, Robert J Wood, Daniela Rus, and Sangbae Kim. «Meshworm: a peristaltic soft robot with antagonistic nickel titanium coil actuators». In: *IEEE/ASME Transactions on mechatronics* 18.5 (2012) (cit. on p. 6).

[16] Huai-Ti Lin, Gary Leisk, and Barry Trimmer. «GoQBot: A caterpillar-inspired soft-bodied rolling robot». In: *Bioinspiration & biomimetics* 6 (June 1, 2011). DOI: `10.1088/1748-3182/6/2/026007` (cit. on pp. 6, 7).

[17] Eric Brown, Nicholas Rodenberg, John Amend, Annan Mozeika, Erik Steltz, Mitchell R Zakin, Hod Lipson, and Heinrich M Jaeger. «Universal robotic gripper based on the jamming of granular material». In: *Proceedings of the National Academy of Sciences* 107.44 (2010) (cit. on p. 6).

[18] Nadia G Cheng, Maxim B Lobovsky, Steven J Keating, Adam M Setapen, Katy I Gero, Anette E Hosoi, and Karl D Iagnemma. «Design and analysis of a robust, low-cost, highly articulated manipulator enabled by jamming of granular media». In: *2012 IEEE international conference on robotics and automation*. IEEE. 2012 (cit. on p. 6).

[19] Yunteng Cao, Masoud Derakhshani, Yuhui Fang, Guoliang Huang, and Changyong Cao. «Bistable Structures for Advanced Functional Systems». In: *Advanced Functional Materials* 31.45 (2021). _eprint: https://advanced.onlinelibrary.wiley.co DOI: `10.1002/adfm.202106231` (cit. on p. 6).

[20] Yinding Chi, Yanbin Li, Yao Zhao, Yaoye Hong, Yichao Tang, and Jie Yin. «Bistable and Multistable Actuators for Soft Robots: Structures, Materials, and Functionalities». In: *Advanced Materials* 34.19 (2022). _eprint: https://advanced.onlinelibrary.wiley.com/doi/pdf/10.1002/adma.202110384. DOI `10.1002/adma.202110384` (cit. on p. 6).

[21] Dong Qin, Younan Xia, and George M Whitesides. «Soft lithography for micro-and nanoscale patterning». In: *Nature protocols* 5.3 (2010) (cit. on p. 6).

[22] Bobak Mosadegh et al. «Pneumatic Networks for Soft Robotics that Actuate Rapidly». In: *Advanced Functional Materials* 24.15 (Apr. 2014). DOI: `10.1002/adfm.201303288` (cit. on p. 7).

[23] Nicholas W Bartlett, Michael T Tolley, Johannes TB Overvelde, James C Weaver, Bobak Mosadegh, Katia Bertoldi, George M Whitesides, and Robert J Wood. «A 3D-printed, functionally graded soft robot powered by combustion». In: *Science* 349.6244 (2015) (cit. on p. 7).

[24] Michael J Motala, Daniel Perlitz, Christopher M Daly, Peixi Yuan, Ralph G Nuzzo, and K Jimmy Hsia. «Programming matter through strain». In: *Extreme Mechanics Letters* 3 (2015) (cit. on p. 7).

[25] Christopher Anderson. «Off like a shot: Scaling of ballistic tongue projection reveals extremely high performance in small chameleons». In: *Scientific Reports* 6 (Jan. 4, 2016). DOI: `10.1038/srep18625` (cit. on p. 8).

[26] Alexis Debray. «Manipulators inspired by the tongue of the chameleon». In: *Bioinspiration & Biomimetics* 6.2 (June 1, 2011). DOI: `10.1088/1748-3182/6/2/026002` (cit. on pp. 9, 16).

[27] Anthony Herrel, Stephen M. Deban, Vicky Schaerlaeken, Jean-Pierre Timmermans, and D. Adriaens. «Are Morphological Specializations of the Hyolingual System in Chameleons and Salamanders Tuned to Demands on Performance?» In: *Physiological and Biochemical Zoology* 82.1 (Jan. 2009). DOI: `10.1086/589950` (cit. on pp. 9, 11, 12).

[28] A. Herrel, J.J. Meyers, K.C. Nishikawa, and F. De Vree. «Morphology and histochemistry of the hyolingual apparatus in chameleons». In: *Journal of Morphology* 249.2 (Aug. 2001). DOI: `10.1002/jmor.1047` (cit. on pp. 9, 10, 13).

[29] Jurriaan H. De Groot and Johan L. Van Leeuwen. «Evidence for an elastic projection mechanism in the chameleon tongue». In: *Proceedings of the Royal Society of London. Series B: Biological Sciences* 271.1540 (Apr. 7, 2004). DOI: `10.1098/rspb.2003.2637` (cit. on pp. 10, 12, 13, 16, 18).

[30] Johan L Van Leeuwen. «Why the chameleon has spiral–shaped muscle fibres in its tongue». In: *Philosophical Transactions of the Royal Society of London. Series B: Biological Sciences* 352.1353 (1997) (cit. on pp. 10, 11).

[31] MJ Rice. «Supercontracting striated muscle in a vertebrate». In: *Nature* 243.5404 (1973) (cit. on p. 10).

[32] Peter C Wainwright, David M Kraklau, and Albert F Bennett. «Kinematics of tongue projection in Chamaeleo Oustaleti». In: (Apr. 22, 1991) (cit. on pp. 12–15, 18).

[33] E Brücke. «Über die Zunge der Chamäleonen». In: *Sitz. Ber. Math.-Nat. Kl. Akad. Wiss., Wien* 8 (1852) (cit. on p. 11).

[34] CP Gnanamuthu. «27. The Anatomy and Mechanism of the Tongue of Chamadeon carcaratus (Merrem)». In: *Proceedings of the Zoological Society of London*. Vol. 100. 2. Wiley Online Library. 1930 (cit. on p. 11).

[35] Peter C. Wainwright and Albert F. Bennett. «The Mechanism Of Tongue Projection In Chameleons: I. Electromyographic Tests Of Functional Hypotheses». In: *Journal of Experimental Biology* 168.1 (July 1, 1992). DOI: `10.1242/jeb.168.1.1` (cit. on pp. 11, 23, 24).

[36] Krystal A. Tolley and Anthony Herrel. *The biology of chameleons*. Berkeley: University of California press, 2013 (cit. on p. 13).

[37] *Shooting Chameleon Tongue in Super Slow Motion | BBC Earth*. In collab. with BBC Earth. Aug. 18, 2017 (cit. on p. 13).

[38] Sunny Kumar, Ishant Tiwari, Victor M. Ortega-Jimenez, Adler R. Dillman, Dongjing He, Yuhang Hu, and M. Saad Bhamla. *Reversible kink instability drives ultrafast jumping in nematodes and soft robots*. June 10, 2024. DOI: `10.1101/2024.06.07.598012` (cit. on pp. 14, 15).

[39] S M Cox, D Schmidt, Y Modarres-Sadeghi, and S N Patek. «A physical model of the extreme mantis shrimp strike: kinematics and cavitation of Ninjabot». In: *Bioinspiration & Biomimetics* 9.1 (Feb. 2014). DOI: `10.1088/1748-3182/9/1/016014` (cit. on p. 15).

[40] Katsushi Kagaya and s Patek. «Feed-forward motor control of ultrafast, ballistic movements». In: *The Journal of experimental biology* 219 (Dec. 8, 2015). DOI: `10.1242/jeb.130518` (cit. on p. 15).

[41] S. N. Patek. «Latch-mediated spring actuation (LaMSA): the power of integrated biomechanical systems». In: *Journal of Experimental Biology* 226 (Suppl_1 Apr. 6, 2023). DOI: `10.1242/jeb.245262` (cit. on p. 16).

[42] Tomofumi Hatakeyama and Hiromi Mochiyama. «Shooting Manipulation Inspired by Chameleon». In: *IEEE/ASME Transactions on Mechatronics* 18.2 (Apr. 2013). DOI: `10.1109/TMECH.2012.2225110` (cit. on p. 16).

[43] Zhilei Zheng, Kun Wang, Xuan Wu, Qiuju Zhang, and Ke Li. «Dynamic Analysis of Elastic Projecting Robot inspired by Chameleon Tongue». In: *2018 IEEE International Conference on Robotics and Biomimetics (ROBIO).* 2018 IEEE International Conference on Robotics and Biomimetics (ROBIO). Kuala Lumpur, Malaysia: IEEE, Dec. 2018. DOI: `10.1109/ROBIO.2018.8664861` (cit. on p. 16).

[44] David Melancon, Antonio Elia Forte, Leon M. Kamp, Benjamin Gorissen, and Katia Bertoldi. «Inflatable Origami: Multimodal Deformation via Multistability». In: *Advanced Functional Materials* 32.35 (2022). _eprint: https://advanced.onlinelibrary.wiley.com/doi/pdf/10.1002/adfm.202201891. DOI: `10.1002/adfm.202201891` (cit. on p. 23).

[45] *Ecoflex™ 00-30 Product Information.* Smooth-On, Inc. URL: `https://www.smooth-on.com/products/ecoflex-00-30/` (visited on 02/27/2026) (cit. on p. 32).

[46] Jörgen Bergström. «Elasticity/Hyperelasticity». In: *Mechanics of Solid Polymers.* Elsevier, 2015. DOI: `10.1016/B978-0-323-31150-2.00005-4` (cit. on pp. 32, 39, 40, 42).

[47] D20 Committee. *Test Method for Tensile Properties of Plastics.* DOI: `10.1520/D0638-14` (cit. on p. 33).

[48] Melvin Mooney. «A theory of large elastic deformation». In: *Journal of applied physics* 11.9 (1940) (cit. on p. 39).

[49] Ronald S Rivlin. «Large elastic deformations of isotropic materials IV. Further developments of the general theory». In: *Philosophical transactions of the royal society of London. Series A, Mathematical and physical sciences* 241.835 (1948) (cit. on p. 39).

[50] Burak Erman and James E Mark. *Structures and properties of rubberlike networks*. Oxford University Press, 1997 (cit. on p. 39).

[51] Jörgen Bergström. «Experimental Characterization Techniques». In: *Mechanics of Solid Polymers*. Elsevier, 2015. DOI: `10.1016/B978-0-323-31150-2.00002-9` (cit. on p. 39).

[52] Oon H Yeoh. «Some forms of the strain energy function for rubber». In: *Rubber Chemistry and technology* 66.5 (1993) (cit. on pp. 40, 42).

[53] Gerhard A Holzapfel. *Nonlinear solid mechanics: a continuum approach for engineering science*. 2002 (cit. on p. 40).

[54] P. A. L. S. Martins, R. M. Natal Jorge, and A. J. M. Ferreira. «A Comparative Study of Several Material Models for Prediction of Hyperelastic Properties: Application to Silicone-Rubber and Soft Tissues». In: *Strain* 42.3 (Aug. 2006). DOI: `10.1111/j.1475-1305.2006.00257.x` (cit. on p. 40).

[55] Christian P Robert, George Casella, and George Casella. *Monte Carlo statistical methods*. Vol. 2. Springer, 2004 (cit. on p. 43).

[56] *smoothdata - Smooth noisy data - MATLAB*. URL: `https://it.mathworks.com/help/releases/R2025b/matlab/ref/smoothdata.html` (visited on 03/09/2026) (cit. on p. 44).

[57] *lsqcurvefit - Solve nonlinear curve-fitting (data-fitting) problems in least-squares sense - MATLAB*. URL: `https://it.mathworks.com/help/optim/ug/lsqcurvefit.html` (visited on 03/10/2026) (cit. on p. 44).

[58] *Altair Optistruct for Nonlinear Analysis - ASEAN - April 2021 (6 hours)*. In collab. with Simulation-Driven Design. June 2, 2021 (cit. on p. 48).

[59] HubSpot. *1106: HyperElastic Material Models - Applications and Usage*. URL: `https://cdn2.hubspot.net/hubfs/47251/HyperWorks_Tips+Tricks_Hyperelastic_Materials.pdf` (visited on 03/10/2026) (cit. on p. 50).

[60] Ramses V. Martinez, Carina R. Fish, Xin Chen, and George M. Whitesides. «Elastomeric Origami: Programmable Paper-Elastomer Composites as Pneumatic Actuators». In: *Advanced Functional Materials* 22.7 (2012). _eprint: https://advanced.onlinelibrary.wiley.com/doi/pdf/10.1002/adfm.201102978. DOI: `10.1002/adfm.201102978` (cit. on p. 65).

[61] Shuguang Li, Daniel M. Vogt, Daniela Rus, and Robert J. Wood. «Fluid-driven origami-inspired artificial muscles». In: *Proceedings of the National Academy of Sciences* 114.50 (Dec. 12, 2017). DOI: `10.1073/pnas.1713450114` (cit. on p. 65).